Article

Spectroscopy and Electronic Structure of Electron Deficient Zinc Phthalocyanines

Steven P. Keizer, John Mack, Barbara A. Bench, Sergiu M. Gorun, and Martin J. Stillman

J. Am. Chem. Soc., **2003**, 125 (23), 7067-7085• DOI: 10.1021/ja0299710 • Publication Date (Web): 16 May 2003

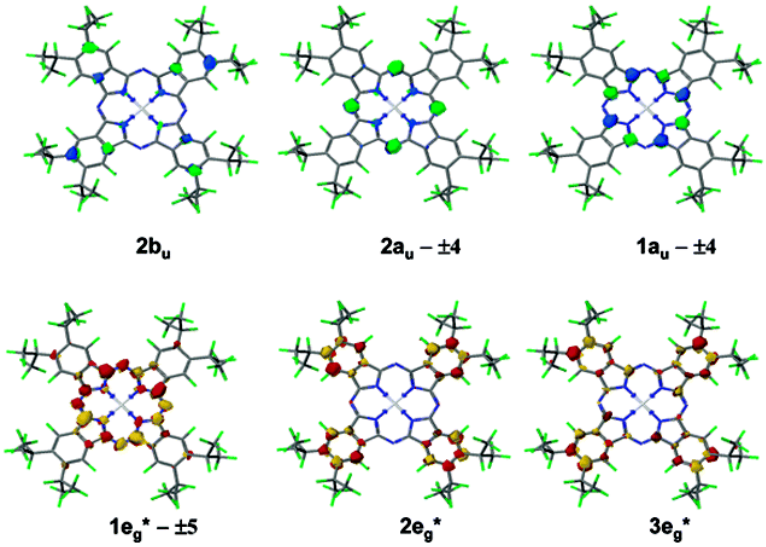

More About This Article

Additional resources and features associated with this article are available within the HTML version:

- Supporting Information
- Links to the 2 articles that cite this article, as of the time of this article download
- Access to high resolution figures
- Links to articles and content related to this article
- Copyright permission to reproduce figures and/or text from this article

View the Full Text HTML

J|A|C|S
ARTICLES
Published on Web 05/16/2003

Spectroscopy and Electronic Structure of Electron Deficient Zinc Phthalocyanines

Steven P. Keizer,† John Mack,† Barbara A. Bench,‡ Sergiu M. Gorun,*,‡ and Martin J. Stillman*,†

Contribution from the Department of Chemistry, The University of Western Ontario, London, Ontario, N6A 5B7 Canada and Department of Chemistry, Brown University, Providence, Rhode Island, 02912

Received December 31, 2002; E-mail: Martin.Stillman@uwo.ca

Abstract: The effect of introduction of perfluoro alkyl groups into phthalocyanines, as evidenced by the spectroscopic properties of 1,4,8,11,15,18,22,25-octa-fluoro-2,3,9,10,16,17,23,24-octa-perfluoro isopropyl zinc phthalocyanine, $ZnF_{64}Pc(-2)$ and its ring-reduced radical anion species, $[ZnF_{64}Pc(-3)]^-$, are reported. A combination of UV−visible absorption and magnetic circular dichroism (MCD) spectroscopy, ESI and MALDI-TOF mass spectrometry, cyclic and differential pulse voltammetry, and complete theoretical calculations using INDO/S and DFT techniques reveals that the substitution of all sixteen hydrogen atoms in protio ZnPc(−2) by eight F and eight *i*-C_3F_7 groups red shifts the Q and $\pi \rightarrow \pi^*$ transitions and narrows the HOMO−LUMO gap while simultaneously preventing ring photooxidation and stabilizing the radical anion. The $[ZnF_{64}Pc(-3)]^-$ species, which is in equilibrium in solution with the neutral complex when a reducing agent is present, is unusually stable. The above effects are attributed to the strong electron withdrawing properties of the peripheral substituents, which render $ZnF_{64}Pc$ extremely electron deficient.

Introduction

The phthalocyanine (or tetraazatetrabenzporphyrin) ligand has a heteroaromatic π-system, Figure 1, and readily forms complexes with main group and transition metals. The aza-nitrogens and peripheral fused benzene rings impart chemical and thermal stability to the ligand. The optical properties of metal phthalocyanine complexes (MPc) have been studied extensively for several decades.[1] The low solubility of these complexes, combined with the intense $\pi \rightarrow \pi^*$ bands associated with the Pc ligand, led to industrial applications as pigments in paints and dyestuffs.[2] In recent decades, there has been renewed interest in the use of MPc complexes in a number of high technology applications, including those based upon the close structural relationship of the phthalocyanines to porphyrin complexes. Mimicking the natural energy cycle of chlorophyll and the oxygen binding and activation properties of the heme proteins, for example, has been a key goal in phthalocyanine research.[3] New applications include as photosensitizers in photodynamic therapy[4] and in anti-scrapie treatments,[5] as power leads[6] and molecular switches in nanotechnology,[7] and as potential industrial catalysts.[8] A rich patent literature covers phthalocyanine applications for optical recording media.

In contrast to uses as pigments, most new applications require enhanced solubility and/or synthetic options for the tuning of the chemical and electronic properties of the MPc complexes. Many desired features could be achieved, in principle, by the addition of peripheral substituents to the Pc ligand. A useful structural modification, the replacement of the C−H bonds of Pc with C−X (halogen) bonds, especially C−F bonds, increases the robustness of the overall ring but does not render the molecules either more soluble or immune to nucleophilic attack.

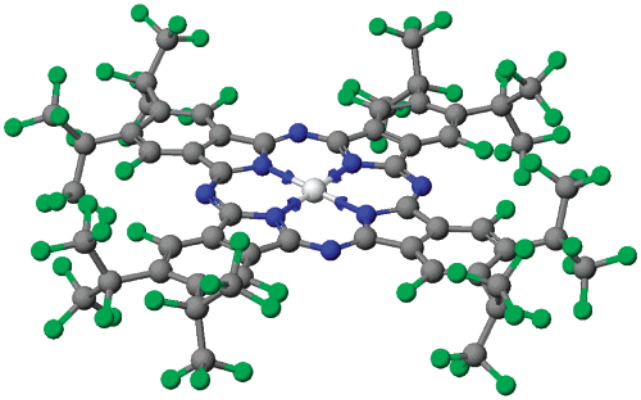

Figure 1. Structure of $ZnF_{64}Pc(-2)$ complex based upon its X-ray coordinates[10] tilted to show the bulkiness of the peripheral fluorinated isopropyl groups. The central metal is zinc. The X-ray analysis showed no deformation from planarity for the inner cyclic polyene ring.

The replacement, at least in part, of the X atoms in the C−X bonds of Pc by *aliphatic* perhalogenated substituents is expected to simultaneously reduce the nucleophilic susceptibility of metallophthalocyanines while enhancing their chemical and thermal robustness. Accordingly, we have shown recently that partial replacement of aromatic F groups by perfluoro isopropyl

† The University of Western Ontario.
‡ Brown University.

(1) (a) Dent, C. E.; Linstead, R. P.; Lowe, A. R. *J. Chem. Soc.* **1934**, 1033−1039. (b) Linstead, R. P.; Robertson, J. M. *J. Chem. Soc.* **1936**, 1195−1209. (c) Linstead, R. P. *J. Chem. Soc.* **1934**, 1016.
(2) Dandridge, A. E.; Drescher, H. A.; Thomas, J. (to Scottish Dyes Ltd.), British Patent 322,169, 1929.

groups in a perfluoro Pc cobalt complex enhances its solubility and promotes novel catalytic oxidation chemistry while preventing the oxidative degradation of the catalyst.[9] The analogous zinc complex, 1,4,8,11,15,18,22,25-octa-fluoro-2,3,9,10,16,17,-23,24-octa-perfluoro isopropyl zinc phthalocyanine, $ZnF_{64}Pc(-2)$, Figure 1, exhibits favorable solubility and photophysical and photodynamic properties.[10] The presence of the eight electron withdrawing perfluoro isopropyl (i-C_3F_7) peripheral R_F substituents imparts resistance toward chemical (including both singlet and triplet dioxygen) and electrochemical oxidation. The presence of the R_F substituents is also expected both to facilitate ring reduction reactions and to stabilize the ring-reduced π-anion radical anion species, such as $[ZnF_{64}Pc(-3)]^-$.[11] Both the neutral and anionic species are likely to be extremely electron deficient, an attribute that should be reflected in their spectroscopic and other features. While we consider in this paper only the case where all hydrogen atoms are removed from a phthalocyanine molecule, partial replacements are known.[12] Such molecules, however, are expected to exhibit a reduced degree of chemical robustness due to residual C−H bonds in either the ring or substituents, while in-depth studies of the electronic structures and properties of their Zn complexes are not reported.

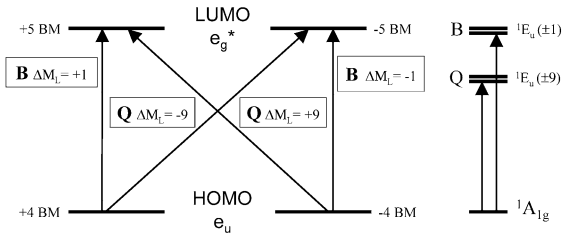

Figure 2. Origins of the absorption and MCD spectral intensities for the first two bands (Q and B) observed in the optical spectra of the porphyrins and phthalocyanines. The Q-band near 670 nm for main group phthalocyanines[11a] exhibits an intense MCD A term that arises from the predicted 9 units of angular momentum. The MCD spectrum of the B band near 330 nm in the phthalocyanines exhibits approximately 1 unit of angular momentum. This four orbital model was described by Gouterman et al.[13,14] and accounts well for the first two major bands, as indicated on the right-hand side of the figure. Detailed spectral analysis of the absorption and MCD spectra data of a range of phthalocyanines[11,16,17] and theoretical interpretation of these data[11] have led to the following sequence of bands (using the nomenclature of Gouterman's model and subsequent modifications by Stillman and co-workers):[11] Q (near 670 nm), second $\pi \rightarrow \pi^*$ (weak near 400 nm), B1 and B2 near 310 nm, and N (near 270 nm). Simplified one-electron origins of these states are shown in Figures 8 and 9.

The interpretation of the optical data in terms of two major transitions between four orbitals was developed theoretically by Gouterman and co-workers and provides an excellent starting point for understanding the spectral data of porphyrins and phthalocyanines,[11,13,14] Figure 2. The presence of changes in angular momentum of, nominally, ±1 and ±9 Bohr magnetons[11,15] results in highly distinctive MCD spectra.[11] Figure 2 shows the origins of the MCD A terms[11,15] observed for two lowest energy bands in both porphyrins and phthalocyanines, the Q and B bands. As we discuss in more detail in the following, the energy separation between the top two highest-occupied molecular orbitals in the metallophthalocyanines means that the formally forbidden Q-band near 670 nm exhibits significant dipole strength as well as a magnetic moment change close to 4 Bohr magnetons.[11,14,15] Analysis of the combined absorption and MCD data, especially of the main group elements, provides definitive assignment criteria to enable the first three−four excited states to be located, as well as providing guidance for theoretical calculations.[16−18]

In this paper, we report the mass spectroscopic and the absorption and magnetic circular dichroism spectral data properties of the $ZnF_{64}Pc(-2)$ and the ring-reduced $[ZnF_{64}Pc(-3)]^-$

(3) (a) Ellis, P. E., Jr.; Lyons, J. E. *Coord. Chem. Rev.* **1990**, *105*, 181 and references therein. (b) Bartoli, J. F.; Brigoud, P.; Battioni, P.; Mansuy, D. *J. Chem. Soc., Chem. Commun*. **1991**, 440. (c) Grinstaff, M. W.; Hill, M. G.; Labinger, J.; Gray, H. B. *Science* **1994**, *264*, 1311. (d) *Metalloporphyrins in Catalytic Oxidations*; Sheldon, R. A., Ed.; Marcel Dekker: New York, 1994. (e) Steinberg-Yfrach, G.; Liddell, P. A.; Hung, S. C.; Moore, A. L.; Gust, D.; Moore, T. A. *Nature* **1997**, *385*, 238−241. (f) Dolphin, D.; Traylor, T. G.; Xie, L. Y. *Acc. Chem. Res.* **1997**, *30*, 251. (g) Steinberg-Yfrach, G.; Riguad, J. L.; Durantini, E. N.; Moore, A. L.; Gust, D.; Moore, T. A. *Nature* **1998**, *392*, 479−482. (h) *Bioinorganic Catalysis*, 2nd ed.; Reedijk, J., Ed.; Marcel Dekker: New York, 1999. (i) *Biomimetic Oxidations*; Meunier, B., Ed.; World Scientific Publishing: London, 2000. (j) Arakawa, H.; Aresta, M.; Armor, J. N.; Barteau, M. A.; Beckman, E. J.; Bell, A. T.; Bercaw, J. E.; Creutz, C.; Dinjus, E.; Dixon, D. A.; Domen, K.; DuBois, D. L.; Eckert, J.; Fujita, E.; Gibson, D. H.; Goddard, W. A.; Goodman, D. W.; Kelle, J.; Kubas, G. J.; Kung, H. H.; Lyons, J. E.; Manzer, L. E.; Marks, T. J.; Morokuma, K.; Nicholas, K. M.; Periana, R.; Que, L.; Rostrup-Nielson, J.; Sachtler, W. M. H.; Schmidt, L. D.; Sen, A.; Somorjai, G. A.; Stair, P. C.; Stults, B. R.; Tumas, W. *Chem. Rev.* **2001**, *101*, 953.

(4) (a) Paquette, B.; Ali, H.; van Lier, E. J. *J. Chim. Phys. Phys.-Chim. Biol.* **1991**, *88*, 1113−23. (b) Boyle, R. W.; Rousseau, J.; Kudrevich, S. V.; Obochi, M. O. K.; van Lier, J. E. *Br. J. Cancer* **1996**, *73*, 49−53. (c) Kaliya, O. L.; Lukyanets, E. A.; Vorozhtsov, G. N. *J. Porphyrins Phthalocyanines* **1999**, *3*, 592−610. (d) Lukyanets, E. *J. Porphyrins Phthalocyanines* **1999**, *3*, 424−432. (e) Allen, C. M.; Sharman, W. M.; van Lier, J. E. *J. Porphyrins Phthalocyanines* **2001**, *5*, 161−169.

(5) Priola, S. A.; Raines, A.; Caughey, W. S. *Science* **2000**, *287*, 1503−1506.

(6) Hersam, M. C.; Guisinger, N. P.; Lyding, J. W. *Nanotechnology* **2000**, *11*, 70−76.

(7) (a) Schlettwein, D.; Karmann, E.; Oekermann, T.; Yanagi, H. *Electrochim. Acta* **2000**, *45*, 4697−4704. (b) Ambroise, A.; Wagner, R. W.; Rao, P. D.; Riggs, J. A.; Hascoat, P.; Diers, J. R.; Seth, J.; Lammi, R. K.; Bocian, D. F.; Holten, D.; Lindsey, J. S. *Chem. Mater.* **2001**, *13*, 1023−1034.

(8) (a) Jasinski, R. *Nature* **1964**, *201*, 1212−1213. (b) Parton, R. F.; Vankelecom, I. F. J.; Casselman, M. J. A.; Bezoukhanova, C. P.; Uytterhoeven, J. B.; Jacobs, P. A. *Nature* **1994**, *370*, 541−544. (c) Balkus, K. J.; Eissa, M.; Levado, R. *J. Am. Chem. Soc.* **1995**, *117*, 10753−10754. (d) Capobianchi, A.; Paoletti, A. M.; Pennesi, G.; Rossi, G.; Caminiti, R.; Ercolani, C. *Inorg. Chem.* **1994**, *33*, 4635−4640. (e) Heron, N. *J. Coord. Chem.* **1988**, *19*, 25. (f) Colonna, S.; Gaggero, N.; Montanari, F.; Pozzi, G.; Quici, S. *Eur. J. Org. Chem.* **2001**, *1*, 181.

(9) Bench, B. A.; Brennessel, W. W.; Lee, H.-J.; Gorun, S. M. *Angew. Chem., Int. Ed.* **2002**, *41*, 750.

(10) (a) Bench, B. A.; Beveridge, A.; Sharman, W. M.; Diebold, G. J.; van Lier, J. E.; Gorun, S. M. *Angew. Chem., Int. Ed.* **2002**, *41*, 748. (b) Bench, B. A. Ph.D. Thesis, Brown University, 2001.

(11) (a) Stillman, M. J.; Nyokong, T. In *Phthalocyanine. Principles and Properties*; Leznoff, C. C., Lever, A. B. P., Eds.; VCH Publications: New York, 1993; Vol. 1, Chapter 3, pp 133−290. (b) Stillman, M. J. In *Phthalocyanine. Principles and Properties*; Lever, A. B. P., Leznoff, C. C., Eds.; VCH Publications: New York, 1993; Vol. 3, Chapter 5, pp 227−296. (c) Mack, J.; Stillman, M. J. *J. Am. Chem. Soc.* **1994**, *116*, 1292−1304. (d) Mack, J.; Stillman, M. J. *J. Phys. Chem.* **1995**, *95*, 7935. (e) Mack, J.; Stillman, M. J. *Inorg. Chem.* **1997**, *36*, 413. (f) Mack, J.; Stillman, M. J. *Coord. Chem Rev.* **2001**, *219*−*221*, 993. (g) Mack, J.; Stillman, M. J. In *Handbook of Porphyrins and Related Macrocycles*; Kadish, K., Smith, K., Guilard, R., Eds.; Academic Press: New York, 2002; Vol. 16, Chapter 103, pp 43−116.

(12) (a) Weitman, H.; Schatz, S.; Gottlieb, H. E.; Kobayashi, N.; Ehrenberg, B. *Photochem. Photobiol*. 2001, *73*, 473. (b) Gao, Qian, X. *J. Fluorine Chem.* **2002**, *113*, 161−165. (c) Sugimori, T.; Horike, S.; Handa, M.; Kasuga, K. *Inorg. Chim. Acta* **1998**, *278*, 253−255. (d) Kondratenko, N. V.; Tretyakova, I. N.; Luk'yanets, E. A.; Volkov, S. V.; Orlova, R. K.; Nemykin, V. N.; Yagupolskii, L. M. *Dyes Pigm.* **1999** *41*, 101−109. (e) Tse, Y.; Kobayashi, N.; Lever, A. B. P. *Collect. Czech. Chem. Commun.* **2001**, *66*, 338.

(13) (a) Gouterman, M. In *The Porphyrins*; Dolphin, D., Ed.; Academic Press: New York, 1978; Vol. III, Part A, pp 1−165. (b) Gouterman, M. *J. Mol. Spectrosc.* **1972**, *44*, 37. (c) Gouterman, M.; Wagniere, G. H.; Snyder, L. C. *J. Mol. Spectrosc.* **1963**, *11*, 108.

(14) (a) McHugh, A. J.; Gouterman, M.; Weiss, C. *Theor. Chim. Acta* **1972**, *24*, 346. (b) Schaffer, A. M.; Gouterman, M.; Davidson, E. R. *Theor. Chim. Acta* **1973**, *30*, 9.

(15) Both the orbital and spin angular moments have associated magnetic moments that can couple with an applied field leading to a splitting of states into $2J + 1$ components. The intensity mechanism for MCD spectroscopy depends on coupling of the ground and excited states through both the electric and magnetic dipole moments. For details, see: (a) Piepho, S. B.; Schatz, P. N. In *Group Theory in Spectroscopy with Applications to Magnetic Circular Dichroism*; Wiley: New York, 1983. (b) Stephens, P. J. *Adv. Chem. Phys.* **1976**, *35*, 197.

(16) (a) Gasyna, Z.; Browett, W. R.; Nyokong, T.; Kitchenham, R.; Stillman, M. J. *Chemom. Intell. Lab. Syst.* **1989**, *5*, 233. (b) Mack, J.; Browett, W.; Stillman, M. J., to be submitted.

species, together with ZINDO and DFT calculations of their respective electronic structures. We compare these data with those reported previously for the nonfluorinated MPc(−2) and $[MPc(-3)]^-$ species.[11] The impact of peripheral substitution on the π-system of the ligand is evidenced by the large changes in the optical spectra of $ZnF_{64}Pc$. Optical spectroscopy is particularly revealing since metal-to-ligand and ligand-to-metal charge transfer bands are not present in the UV−visible spectrum of ZnPc(−2). We report the second complete analysis of an MCD spectrum of a phthalocyanine anion radical measured at room and low temperatures.

Materials and Methods

1,4,8,11,15,18,22,25-octa-fluoro-2,3,9,10,16,17,23,24-octa-perfluoro isopropyl zinc phthalocyanine, $ZnF_{64}Pc(-2)$, was synthesized and purified as reported previously.[9,10] Spectrograde dimethylformamide (DMF) (Fischer Scientific) and dimethylacetamide (DMA) (Aldrich), hydrazine hydrate (Aldrich), and CBr_4 (Kodak) were used as supplied. LiCl (Kodak) was recrystallized before use as an electrolyte. Photoreduction of $ZnF_{64}Pc(-2)$ was carried out in a 1% v/v hydrazine hydrate/DMF solution using a 300 W tungsten−halogen Kodak projector lamp fitted with a Pyrex filter. Photooxidation of the $[ZnF_{64}Pc(-3)]^-$ radical anion species was carried out using a 0.01 M solution of CBr_4 as the electron acceptor.[11c,19]

Mass Spectrometry. Electrospray ionization mass spectrometry (ESI-MS) was carried out on DMF solutions of $ZnF_{64}Pc(-2)$ using a Sciex API 365 mass spectrometer. A Hamilton 250 μL syringe was used to provide an infusion rate of 2 μL min^{-1}. The mass spectrometer was operated in the negative ion mode at a potential of −5400 V at the ionization tip. Calibration was carried out using a standard solution of polypropylene glycol (PPG). Matrix assisted laser desorption ionization with time-of-flight detection mass spectrometry (MALDI-TOF) data were acquired on a Micromass TofSpec 2E mass spectrometer (Wythenshawe, Manchester, U.K.) in the negative ion mode. A 1 mg/mL $ZnF_{64}Pc(-2)$ acetone solution and a 10 mg/mL matrix of α-cyano-4-hydroxycinnamic acid were mixed 1:1 prior to application on the target. The samples were analyzed in reflection mode, and the MS data were externally calibrated with a peptide mix (bradykinin, angiotensin I, renin substrate and ACTH18-39).

Optical Spectroscopy. A. Absorption Spectroscopy. Room temperature spectra were recorded in degassed, argon-saturated DMF solutions with a Cary 5 spectrophotometer using the software package supplied by Varian. Absorption spectra were measured at liquid nitrogen temperatures in an Oxford Instruments CF-204 gas flow optical cryostat mounted in the sample compartment of an AVIV 17-DS spectrophotometer using the Aviv software package and a specially designed optical cell.[17f]

B. MCD Spectroscopy. Room temperature MCD spectra were recorded with an Oxford Instruments SM2 superconducting magnet with a 5.1 T field, mounted in the sample compartment of a Jasco J-810 CD spectropolarimeter. Data were recorded under the control of an PC computer using the Spectramanager program of Jasco Inc. A $CoSO_4$ solution was used to calibrate the field strength. Low temperature spectra were recorded using optically transparent vitrified solutions of a DMF/DMA (~90/10%) solvent mixture, where an Oxford Instruments SM4 superconducting magnet (0−5 T) was mounted in the sample compartment of a Jasco J-500C spectrometer for measuring low temperature MCD spectra using the same vitreous solutions and optical cells at 40 K with a magnetic field of 1.6 T.

Electrochemistry and Spectroelectrochemisty. The electrochemical experiments were performed in DMF, with LiCl, 0.1M, as the supporting electrolyte, using a Princeton Applied Research model 273 potentiostat and the VOLTAMSCAN program running on an IBM 9000 computer.[17a,19] The working and auxiliary electrodes were constructed of platinum plates, with an area of 40 mm^2. Ag/AgCl was the reference electrode. Scan rates of 50 mV/s and 5 mV/s were used to record the cyclic voltammogram and the differential pulse voltammogram, respectively. Spectroelectrochemisty was carried out in a cell with a specially designed cell cap, with a nitrogen purge, along with working, auxiliary, and reference electrode contacts. The AVIV 17-DS spectrophotometer was used to obtain the UV−visible data.

Electron Paramagnetic Resonance Spectroscopy. The electron paramagnetic resonance (EPR) spectrum of $[ZnF_{64}Pc(-3)]^-$ was recorded on a Bruker 300 X-band spectrometer at 77 K in a liquid nitrogen Dewar. $[ZnF_{64}Pc(-3)]^-$ was prepared photochemically, as described previously, in a DMF/hydrazine solution at room temperature and was subsequently quenched in liquid nitrogen.

Spectral Band Deconvolution. The SIMPFIT program allows spectral band deconvolution of extensively overlapped spectral envelopes.[11g,16] The major problem associated with band deconvolution analyses is that many different potential fits of Gaussian shaped bands can usually be obtained for a single spectral data set. SIMPFIT overcomes this problem by calculating an experimental spectrum that matches both the MCD and absorption spectral data sets recorded for the same solution. The MCD signal arises from the same electronic transitions as the UV−visible absorption spectrum, but the selection rules are different, as the intensity mechanism depends on the magnetic dipole moment, in addition to the electric dipole moment.[11,15] The band morphologies, however, are different as the applied external magnetic field has a significant impact on the orbital and spin degeneracy of electronic states. The Faraday A, B, and C terms have been assigned considering that the derivative-shaped A term, which identifies degenerate excited states, is temperature independent, while the Gaussian-shaped C term, which identifies an orbitally degenerate ground state, is highly temperature dependent. The temperature independent B terms, which arise from mixing between closely related states linked by a magnetic dipole transition moment, is also Gaussian shaped.[11,15] The B and C terms can have either a positive or negative intensity. The sign of the A term is related to whether the positive or negative portion of the derivative-shaped signal occurs at higher energy. The MCD spectrum in the visible (Q-band) region of symmetric metallophthalocyanines is dominated by a positive A term centered on the Q-band near 670 nm. When this degeneracy is broken, two coupled B terms of opposite signs maintain the same alternating sequence in signs as the A term, but with greatly diminished signal intensity.

Under the rigid shift assumption, the application of a magnetic field makes no difference to the spectral band shape function.[15a] Data recorded at cryogenic temperatures on vitreous solutions are better suited for use with the SIMPFIT program than room temperature data. Solvation effects broaden absorption bands recorded at room temperature to a more significant extent than is the case in the MCD spectrum due to the different selection rules associated with the two techniques.[11d,g] When spectra are measured from vitrified solution, close agreement is observed in absorption and MCD bandwidths, since hot bands associated with vibrational levels of the ground state are frozen out. Obtaining a

(17) (a) Nyokong, T.; Gasyna, Z.; Stillman, M. J. *Inorg. Chem.* **1987**, *26*, 548. (b) Nyokong, T.; Gasyna, Z.; Stillman, M. J. *Inorg. Chem.* **1987**, *26*, 1087. (c) Ough, E. A.; Nyokong, T.; Creber, K. A. M.; Stillman, M. J. *Inorg. Chem.* **1988**, *27*, 2724. (d) Ough, E. A.; Gasyna, Z.; Stillman, M. J. *Inorg. Chem.* **1991**, *30*, 2301. (e) Gasyna, Z.; Stillman, M. J. *Inorg. Chem.* **1990**, *29*, 5101. (f) Mack, J. Ph.D. Thesis, University of Western Ontario, 1992. (g) Nyokong, T. N. Ph.D. Thesis, University of Western Ontario, 1986. (h) Ough, E. A. Ph.D. Thesis, University of Western Ontario, 1992.
(18) (a) Henriksson, A.; Roos, B.; Sundbom, M. *Theor. Chim. Acta* **1972**, *27*, 303. (b) Dedieu, A.; Rohmer, M.-M.; Veillard, A. *Adv. Quantum Chem.* **1982**, *16*, 43. (c) Orti, E.; Bredas, J. L.; Clarisse, C. *J. Chem. Phys.* **1990**, *92*, 1228. (d) Liang, X. L.; Flores, S.; Ellis, D. E.; Hoffman, B. M.; Musselman, R. L. *J. Chem. Phys.* **1991**, *95*, 403. (e) Rosa, A.; Baerends, E. J. *Inorg. Chem.* **1992**, *31*, 4717. (f) Rosa, A.; Baerends, E. J. *Inorg. Chem.* **1994**, *33*, 584. (g) Ishikawa, N.; Ohno, O.; Kaizu, Y.; Kobayashi, H. *J. Phys. Chem.* **1992**, *96*, 8832. (h) Ishikawa, N.; Ohno, O.; Kaizu, Y. *J. Phys. Chem.* **1993**, *97*, 1004. (i) Liao, M.-S.; Scheiner, S. *J. Chem. Phys.* **2001**, *114*, 9780. (j) Ricciardi, G.; Rosa, A.; Baerends, E. J. *J. Phys. Chem. A.* **2001**, *105*, 5242.
(19) Keizer, P. S.; Han, W.; Stillman, M. J. *Inorg. Chem.* **2002**, *41*, 353.

satisfactory fit for two spectra with very different band morphologies using the same basic band parameters removes much of the ambiguity that is normally associated with spectral band deconvolution analysis. An updated version of SIMPFIT[11g,16b] developed using Visual Basic was used for the band fitting reported in this paper.

ZINDO, DFT, and MOPAC Molecular Orbital Calculations. All calculations were performed using CAChe WorkSystem Pro Version 5 software (Fujitsu America).[20] The starting structures were developed through the use of the Workspace module of the CAChe workstation software[20] and were refined at the Restricted Hartree−Fock self-consistent field (SCF) level[21] using the ZINDO program in the CAChe software package.[22,23] These SCF optimizations were carried out at the intermediate neglect of differential overlap/[24] (INDO/1) level of approximation. Structures were then optimized by a density functional theory (DFT) calculation using the B88-PW91 GGA functional with DZVP basis sets or through ground state geometry calculation based on eigenfollowing optimization. UV−visible absorption spectra were then calculated using the spectroscopic INDO Hamiltonian (INDO/s).[22,23]

Results

The chemical and photochemical effects of the significant electron withdrawing properties of the fluorinated isopropyl peripheral substituents[9,10,19] dramatically move the electronic equilibrium toward the ring-reduced species. The effect of this move in charge toward the periphery is observed in the mass spectral data and in the electrochemical data, through the ease of forming the ring-based, π anion radical. Because the energies of the molecular orbitals are disturbed so much from the unsubstituted ZnPc(−2), we have an opportunity to test theoretical predictions using ZINDO/S techniques in which states defined by their polarization properties can be identified in the MCD spectral data.

Electrospray ionization mass spectrometry provides direct structural information about the species present in solution, information that cannot be obtained from optical spectroscopy or, in many cases, from more traditional electron ionization mass spectrometery where the sample is vaporized first. The ESI-MS spectrum of the $ZnF_{64}Pc(-2)$ complex dissolved in DMF is shown in Figure 3. Two main signals are measured for this solution, at 1050 *m*/*z* and at 2101 *m*/*z*, panel A in Figure 3.[25] The signal at 1050 *m*/*z* is assigned to $[(Cl^-)ZnF_{64}Pc(-3)]^-$, which is in equilibrium in solution with $(Cl^-)ZnF_{64}Pc(-2)$. The origin of the Cl^- ion is unknown at this time. It could simply be a low-level contaminant, considering that typical concentrations of $ZnF_{64}Pc$ are at the micromolar level. The parent ion mass in each case included mass and charge of the chloride ion. The spectrum of panel B was obtained from a solution of $(Cl^-)ZnF_{64}Pc(-2)$ that had undergone photoreduction to $[(Cl^-)ZnF_{64}Pc(-3)]^-$ according to eq 1:

$$(Cl^-)ZnF_{64}Pc(-2) + N_2H_4{\cdot}H_2O + h\nu \rightarrow [(Cl^-)ZnF_{64}Pc(-3)]^- + \text{hydrazine radical products} \quad (1)$$

The photoreduction is complete, as evidenced by the observation of only the 1050 *m*/*z* peak of $[(Cl^-)ZnF_{64}Pc(-3)]^-$. It appears that the perfluoro peripheral substituents withdraw electron density from the inner ring and the central metal, so that axial ligation is enhanced relative to the parent $ZnF_{64}Pc(-2)$ complex, as exemplified by the binding of Cl^-. The presence of the anion radical was confirmed by the EPR spectrum of the previous solution, which exhibits a $g \approx 2.009$ signal at liquid nitrogen temperatures, Figure 7. The photoreduction is reversible.

The radical anion was photooxidized using CBr_4 as the electron acceptor, according to eq 2:

$$[(Cl^-)ZnF_{64}Pc(-3)]^- + CBr_4 + h\nu \rightarrow (Cl^-)ZnF_{64}Pc(-2) + Br^- + \text{other radical products} \quad (2)$$

As shown in the resultant mass spectrum (Figure 3, panel C), the anion radical peak is completely absent following the photoinduced oxidation. The MALDI-TOF-MS data for $ZnF_{64}Pc(-2)$, Figure 4, reveal a signal in the mass range for $ZnC_{56}F_{64}N_8$ (2065.97 amu), consistent with the FAB mass spectrum,[10] as well as a second set of peaks at ∼2101 amu, which corresponds to the chloride, $(Cl^-)ZnF_{64}Pc(-2)$.[19] These assignments have been confirmed by a comparison with the corresponding calculated isotopic distribution patterns (B and D of the inset in Figure 4). The presence of the Cl^- anion in the mass spectrum suggests that Zn(II) preferentially binds the adventitious chloride forming a 5-coordinate species. Unlike the case of the anion, attempts to photochemically oxidize $ZnF_{64}Pc(-2)$ to form the radical cation $[ZnF64Pc(-1)]^+$ species proved unsuccessful. There is evidence, however, that, in the presence of strong electron donating ligands, such as imidazole, $ZnF_{64}Pc(-2)$ can be oxidized electrochemically.[10]

Cyclic and differential pulse voltammetry indicate that the reduction of the $ZnF_{64}Pc(-2)$ complex is much easier than in the case of ZnPc(−2), Figure 5. The first reduction potential for $ZnF_{64}Pc(-2)$ is at −630 mV versus SHE (−430 mV vs Ag/AgCl), being fully reversible, while the second irreversible reduction occurs at −1120 mV (−920 mV vs Ag/AgCl). The corresponding potentials for ZnPc are −950 mV and −1450 mV vs SHE,[26] very much more negative.

The electrochemical reduction of $(Cl^-)ZnF_{64}Pc(-2)$ in DMF is accompanied by systematic changes in the UV−visible spectrum, Figure 6, that are associated with radical anion formation.[11c,f] The increase of the potential from −50 mV to

(20) *CAChe Worksystem Pro*, version 5; CAChe Scientific: P.O. Box 500, Mail Station 13-400 Beaverton, OR 97077.
(21) Roothaan, C. C. J. *Rev. Mod. Phys.* **1951**, *23*, 69
(22) (a) Ridley, J. E.; Zerner, M. C. *Theor. Chim. Acta* **1973**, *32*, 111. (b) Zerner, M. C.; Loew, G. H.; Kirchner, R. F.; Mueller-Westerhoff, U. T. *J. Am. Chem. Soc.* **1980**, *102*, 589. (c) Ridley, J. E.; Zerner, M. C. *Theor. Chim. Acta* **1976**, *42*, 223. (d) Bacon, A.; Zerner, M. C. *Theor. Chim. Acta* **1979**, *53*, 21.
(23) (a) Head, J.; Zerner, M. C. *Chem. Phys. Lett.* **1985**, *122*, 264. (b) Head, J.; Zerner, M. C. *Chem. Phys. Lett.* **1986**, *131*, 359. (c) Anderson, W.; Edwards, W. D.; Zerner, M. C. *Inorg. Chem.* **1986**, *25*, 2728. (d) Edwards, W. D.; Zerner, M. C. *Theor. Chim. Acta* **1987**, *72*, 347. (e) Kotzian, M.; Roesch, N.; Zerner, M. C. *Theor. Chim. Acta* **1992**, *81*, 201. (f) Kotzian, M.; Roesch, N.; Zerner, M. C. *Int. J. Quantum Chem.* **1991**, 545.
(24) Pople, J. A.; Beveridge, D.; Dobash, P. A. *Chem. Phys.* **1967**, *47*, 2026.
(25) We use nomenclature designed to unambiguously define the charge on both the ring and the metal. The phthalocyanine ring is a dianion, so when written as MPc(−2), with a divalent metal such as Zn(II), we imply the neutral $[MPc]^0$ complex. In the case of ring-reduced or oxidized radical species, Pc(−3) and Pc(−1) denotes the charge on the ring, while the overall charge of the complex is indicated by square brackets, so the ring-oxidized radical cation is $[ZnPc(-1)]^+$, whereas the ring-reduced, radical anion is $[ZnPc(-3)]^-$. When a specific axial ligand is known to be present, it is included within the brackets. This is not a problem with neutral ligands such as pyridine. However, we are in this paper writing about an MPc cation radical species axially ligated with X^- as, therefore, $[(X^-)MPc(-1)]^+$, which means that the overall charge shown is emphasizing the redox state of the ring rather than the sum of the ring, metal, and axial ligand. For the ring-reduced anion radical, we write the complex as $[(Cl^-)(MPc(-3)]^-$ ignoring the charge on the coordinated chloride to emphasize the charge on the ring (here with 19 π electrons). We hope that this scheme allows the key redox states of the ring to be seen as in this case; it is the number of ring π electrons, 17, 18, or 19, that is determining the observed properties.
(26) Louati, A.; El Mercy, M.; Andre, J. J.; Simon, J.; Kadish, K. M.; Gross, M.; Giraudeau, A. *Inorg. Chem.* **1984**, *23*, 5.

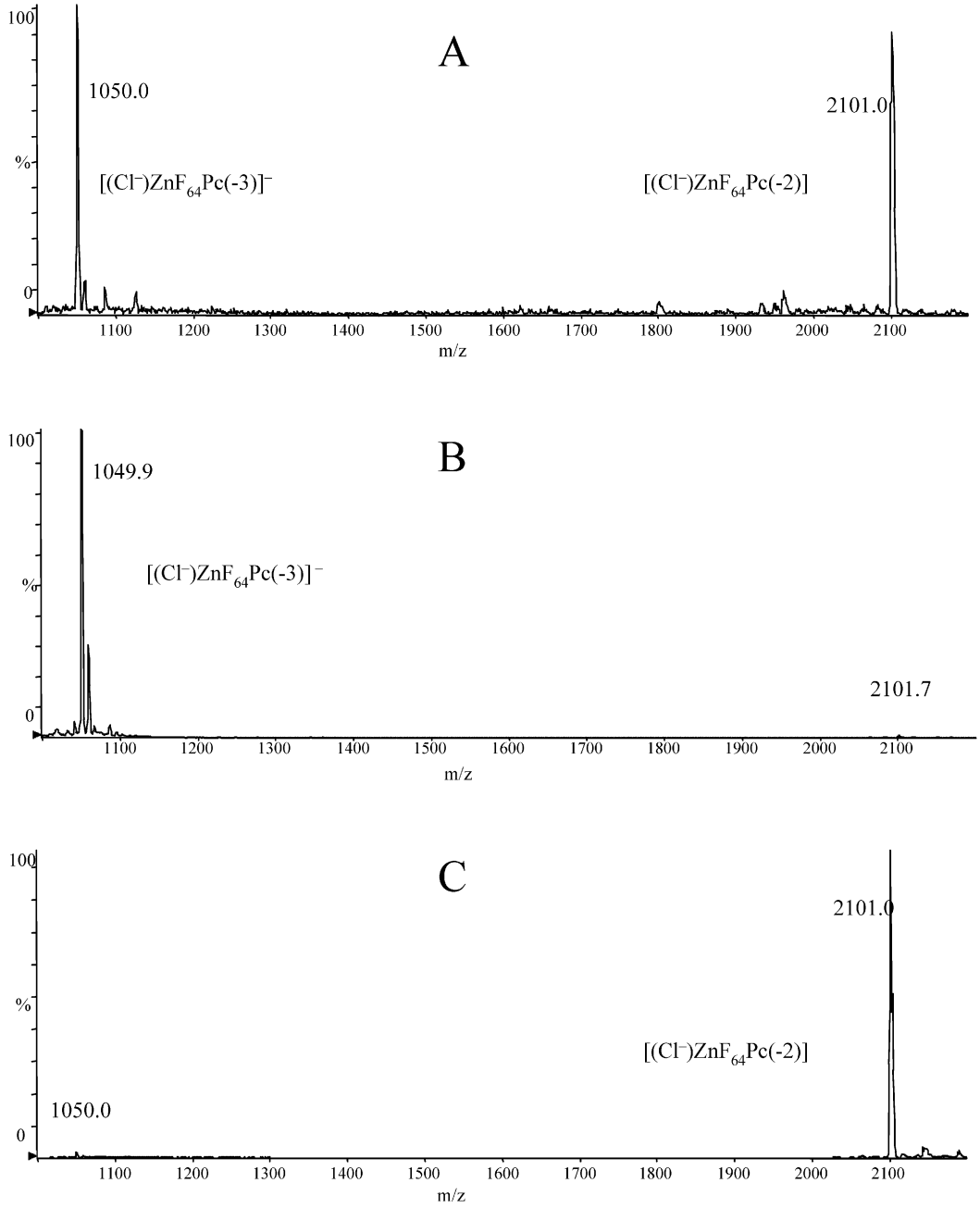

Figure 3. Electrospray ionization MS data for a DMF solution of $ZnF_{64}Pc(-2)$. (A) Direct infusion of a sample of crystalline $ZnF_{64}Pc(-2)$ dissolved in DMF. The ion at 1050 *m/z* corresponds to the doubly charged $[(Cl^-)ZnF_{64}Pc(-3]^-$ ring-reduced, radical anion; the ion at 2101 *m/z* corresponds to $(Cl^-)ZnF_{64}$-$Pc(-2)$. (B) The only peak measured following photochemical reduction of the sample using hydrazine hydrate as the electron donor, this mass corresponds to a parent ion of $[(Cl^-)ZnF_{64}Pc(-3)]^-$. (C) The same solution used for panel B following photooxidation using CBr_4 as the electron acceptor. The peak corresponds to $(Cl^-)ZnF_{64}Pc(-2)$. See the nomenclature described in ref 25.

-500 mV in 50 mV steps, with 30 min equilibrium times, results in the gradual formation of the $[ZnF_{64}Pc(-3)]^-$ radical anion, with band maxima at 468, 594, and 743 nm. No bands of longer wavelength were observed. This solution can be readily oxidized electrochemically to regenerate $(Cl^-)ZnF_{64}Pc(-2)$ in almost 100% yield.

Figure 7 shows EPR data recorded at 77 K for a sample of $ZnF_{64}Pc(-2)$ that had been photochemically reduced to the $[ZnF_{64}Pc(-3)]^-$ radical anion with hydrazine hydrate as the electron donor according to reaction 1. The $g = 2.009$ center point identifies a ring-based radical. These data confirm that the radical anion species is monomeric at room temperature because the radical is detected at low temperatures in both the EPR and MCD (in the following) experiments.

To describe the spectral features of the neutral $ZnF_{64}Pc(-2)$ and, later, the ring-reduced $[ZnF_{64}Pc(-3)]^-$ anion radical, we first describe a model based on analysis of the absorption and MCD data of $ZnPc(-2)$ and its oxidized and reduced species,[11] together with detailed ZINDO/S and DFT calculations. Figure 8 shows one-electron transitions between the ring$-\pi$ MOs that form the largest fraction of the lowest five excited states. In addition, the origins of two weaker bands are shown, namely, the n $\rightarrow \pi^*$ and the second $\pi \rightarrow \pi^*$ bands that lie between 650 and 350 nm.[11d] It is important to note that the introduction of

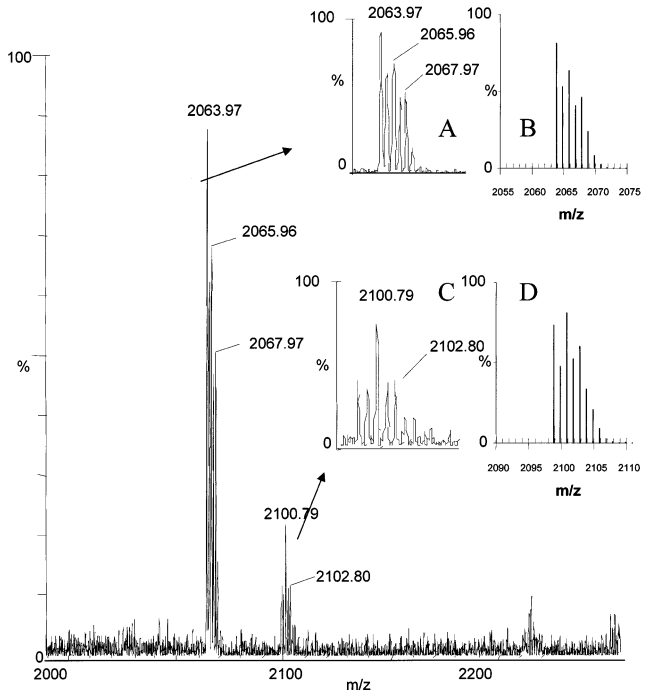

Figure 4. MALDI-MS data for a crystalline sample of $ZnF_{64}Pc(-2)$ using the conditions described in the Materials and Methods section. The mass spectrum shows two major band centers, at 2064 and 2101 *m*/*z*. (A) Observed isotopic pattern for $ZnF_{64}Pc(-2)$ at 2064 *m*/*z* and (B) predicted isotopic pattern. (C) Observed isotopic pattern for $(Cl^-)ZnF_{64}Pc(-2)$ at 2101 *m*/*z* and (D) predicted isotopic pattern.

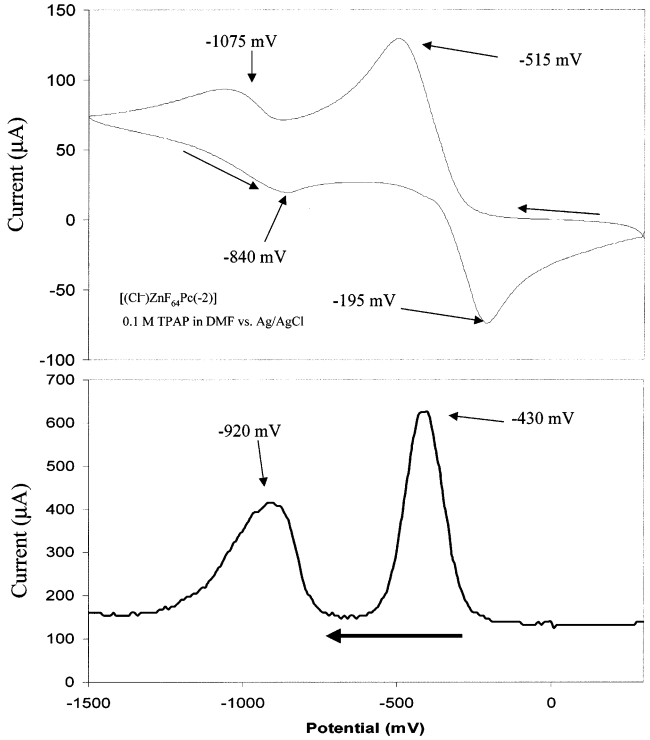

Figure 5. Cyclic voltammogram (CV) (top) and differential pulse voltammogram (DPV) (bottom) of a DMF solution of $(Cl^-)ZnF_{64}Pc(-2)$. The electrolyte was 0.1 M TPAP with a reference electrode of Ag/AgCl. Under these conditions, only the two reduction potentials shown (−430 and −920 mV vs Ag/AgCl, and when corrected to the SHE, these values are −630 and −1120 mV, respectively) were observed. No oxidation potentials could be detected.

the aza-nitrogens and the fused benzene groups that change a porphin ring into a phthalocyanine ring result in the appearance

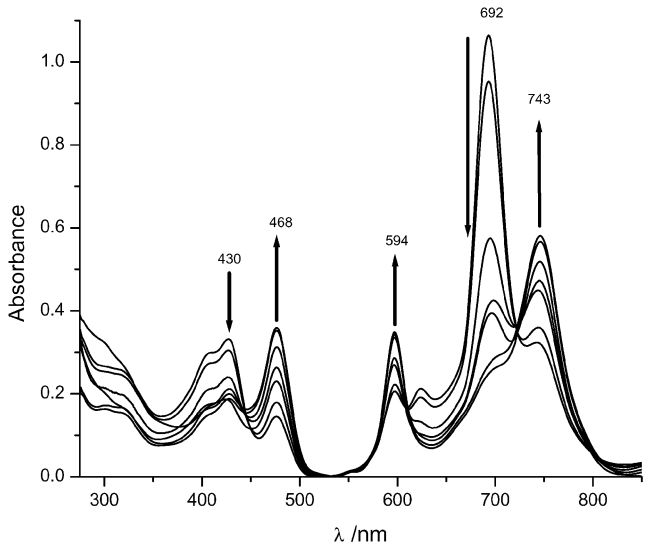

Figure 6. Spectroelectrochemical reduction of $(Cl^-)ZnF_{64}Pc(-2)$ to $[(Cl^-)ZnF_{64}Pc(-3)]^-$ in DMF using an electrolyte of 0.1 M LiCl. The wavelengths marked indicate the band maxima for $(Cl^-)ZnF_{64}Pc(-2)$ and $[(Cl^-)ZnF_{64}Pc(-3)]^-$.

of a large number of additional molecular orbitals. The dotted line box in Figure 8 shows the 4-orbitals of the Gouterman model[13,14] outlined in Figure 2. As we will show below in new calculations reported in this paper for the peripherally substituted phthalocyanine, these four orbitals retain their identity despite the major perturbations invoked by the peripheral substitutions of the fluorinated isopropyl groups. Figure 9 shows the one-electron description of the lowest energy states for the one-electron, ring-reduced anion radical $[ZnPc(-3)]^-$.[11e−g] The key change here is that the spectroscopic evidence from the analysis of the low temperature MCD spectra of the unsubstituted $[ZnPc(-3)]^-$ proves that the ground state is nondegenerate.[11c] The lack of MCD A terms in the $[ZnPc(-3)]^-$ spectral data[11c] is unambiguous evidence that the geometry of the ring is highly distorted. Transition are expected for $\pi \rightarrow \pi^*$ and $\pi^* \rightarrow \pi^*$ molecular orbitals as shown. The $\pi \rightarrow \pi^*$ transitions will retain their Q, B1, and B2 characteristics but with significant changes in energy and band intensities due to the presence of the electron in the π^* excited state. Overlaid on the $\pi \rightarrow \pi^*$ set of transitions will be new transitions assigned as $\pi^* \rightarrow \pi^*$. A key assignment criterion will be the alternating +/− sign of the MCD bands as the B terms arise from the splitting of degenerate states, so the B terms will resemble split positive A terms.

The room temperature absorption and MCD spectra for $ZnF_{64}Pc(-2)$ in DMF are shown in Figure 10. The lowest energy $\pi \rightarrow \pi^*$ band (the Q-band arising from the $1a_{1u} \rightarrow 1e_g^*$ transition), Figure 8, shifts to the red relative to ZnPc, from 670 to 692 nm. The intense positive A term followed by the vibronic bands to higher energy[11d] is typical for a main group phthalocyanine.[11a,f,g] Because there are no possible charge transfer transitions, the 450−600 nm region is transparent. The 300−450 nm region is much more complicated in the case of the perfluoro derivative than observed for the $ZnPc(-2)$ species.[17] In the case of "regular", main group $(L)_nMPc(-2)$ complexes, there are two intense, overlapping, positive A terms in the MCD spectrum named the B1 and B2 bands, Figure 8,[11a,17] that arise primarily from transitions from $1a_{1u}$ and $1b_{1u}$ into the $1e_g^*$ LUMO. In porphyrin complexes, the $1a_{1u}$ and $1a_{2u}$ HOMOs are nearly

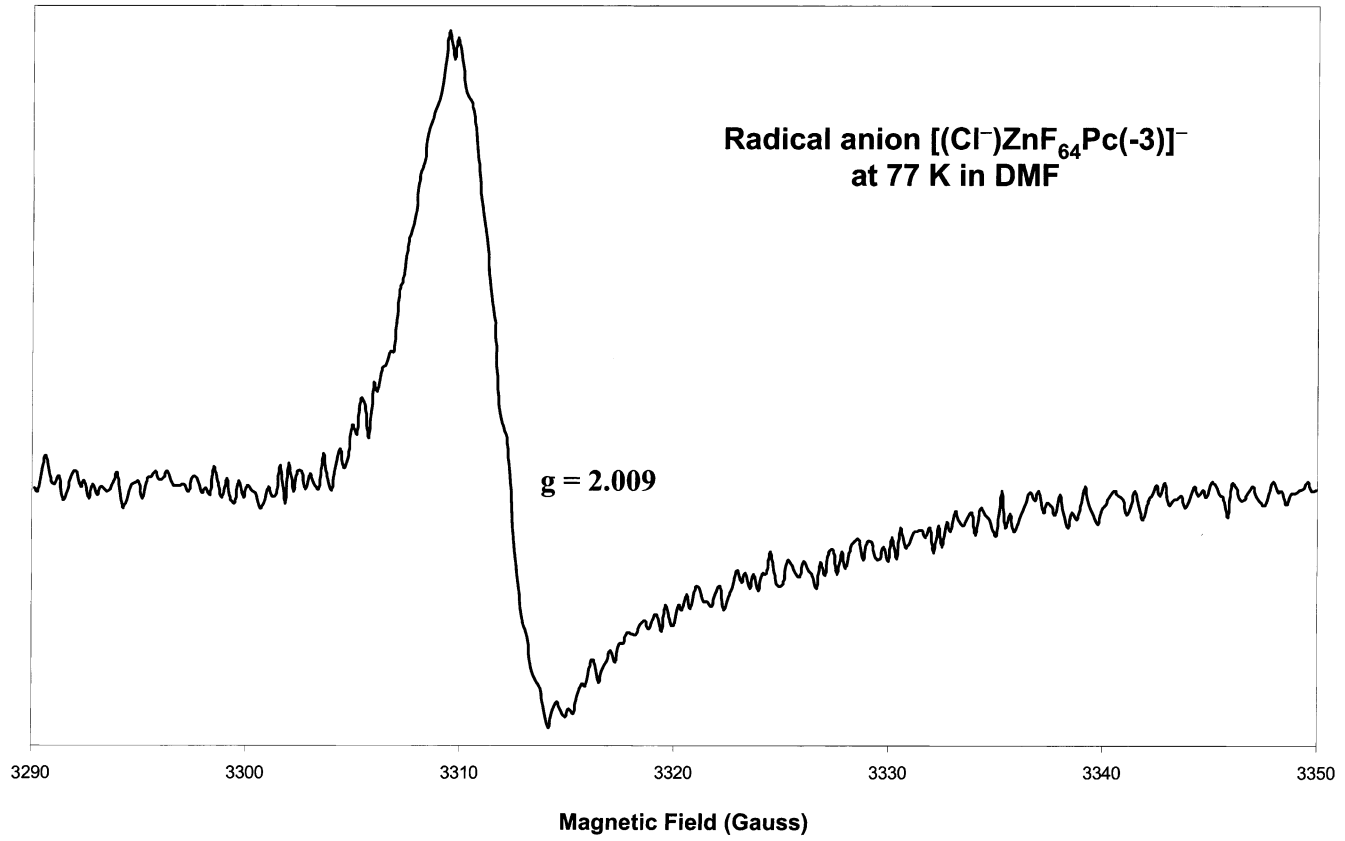

Figure 7. EPR spectrum (77 K) of $[ZnF_{64}Pc(-3)]^-$, generated photochemically in DMF in the presence of hydrazine hydrate. The band is centered on $g = 2.009$.

degenerate and are well separated in energy terms from the $1b_{1u}$ MO, so the B2 band is only observed in the case of the phthalocyanines. The bands within the B1/B2 region are generally not well resolved and often can only be identified by band deconvolution that couples the absorption and MCD spectral data.[11a,g,17] In the case of the MCD spectrum of $(Cl^-)ZnF_{64}Pc(-2)$, Figure 10, it is clear that there are two overlapping, positive A terms centered on the two maxima in the absorption; the complete fits for the perfluoro complex are described in the following section.

The major effect of the 64 F substituents is a significant red shift of the first intense UV-region band to 430 nm (with the negative maximum of the MCD band at 436 nm). The low temperature absorption spectrum, which was obtained using a vitrified DMF/DMA solution at 77 K, Figure 10 (dotted line), shows significant sharpening of all the bands but no new bands or significant shifts in band maxima. While sharpening was observed in the low temperature MCD spectrum, which is dominated by A terms, no significant temperature dependence was observed in the MCD intensity, which is consistent with the expectation that the ground states of this divalent, main group D_{4h} MPc(−2) complexes are $^1A_{1g}$, while the accessible $\pi \rightarrow \pi^*$ excited states are ^1E_u (x/y polarized). The UV−visible absorption (at 298 and 77 K) and MCD (at 298 and 40 K) spectra of photoreduced $[(Cl^-)ZnF_{64}Pc(-3)]^-$ are shown in Figure 11. The major features in the absorption spectrum of the anion radical are similar to those reported previously for $[ZnPc(-3)]^-$,[11c] notably three sets of bands are prominent in the wavelength ranges (unsubstituted $[ZnPc(-3)]^-$ wavelength ranges in parentheses) 350−500 nm (383−434 nm), 500−650 nm (569−635 nm), and 650−900 nm (800−1000 nm). Missing from the absorption data of $[(Cl^-)ZnF_{64}Pc(-3)]^-$ are the weak bands near 950 nm identified as the Q-band in the spectra of $[ZnPc(-3)]^-$.[11c]

The MCD data are essential in providing a guide to the assignment of these absorption bands. As we will see later in the Discussion, analysis of the MCD data and correspondence with the results of the ZINDO/S calculations indicate that the bands between 350 and 500 nm are $\pi \rightarrow \pi^*$ transitions to the B1 and B2 states and the bands between 550 and 900 nm arise from red shifted $\pi^* \rightarrow \pi^*$ transitions. The lack of any appreciable absorption out to 2000 nm, strongly suggests that the $\pi \rightarrow \pi^*$ Q-band lies near 800 nm and is masked by the more intense $\pi^* \rightarrow \pi^*$ transitions. The low temperature MCD data, shown as a dotted line in Figure 11, provides unambiguous evidence that the ground state is nondegenerate and that the spectrum is dominated by B terms rather than C terms expected for a configuration based on a degenerate $1e_g^*$ LUMO [e.g., $((1a_{2u})^2\ (1a_{1u})^2\ ((1e_g^*)^2)$. Similar to the spectral data reported previously for nonfluorinated $[ZnPc(-3)]^-$,[11c] the MCD signal intensity was found to be temperature independent over the range 298−40 K. The EPR data provides confirmation that the unpaired electron in the Jahn−Teller split $1e_g^*$ LUMO is not spin paired, as it would be if the molecule existed as a dimer.

ZINDO, DFT, and MOPAC Molecular Orbital Calculations. Geometry optimization calculations were performed on 1,4,8,11,15,18,22,25-F,2,3,9,10,16,17,23,24-C_2F_5 ZnPc, a $ZnF_{48}Pc$ model complex for $ZnF_{64}Pc$ due to memory related limitations of the CAChe ZINDO and DFT computation

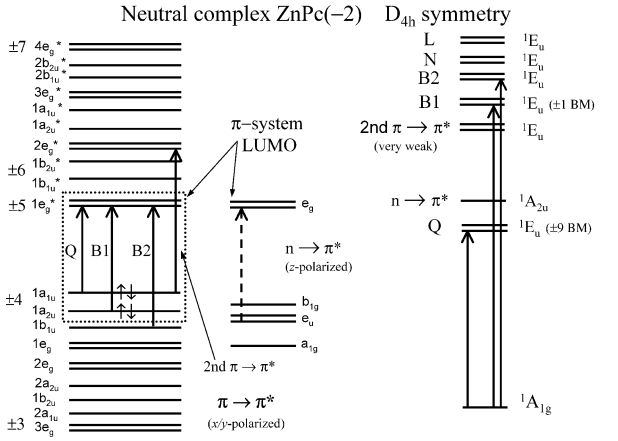

Figure 8. Molecular orbital diagram of ZnPc(−2) showing the transitions that are predicted to give rise to absorption bands in the 280−1000 nm range of the optical spectrum, including the prediction of MCD A terms. The orbital ordering is based on current ZINDO calculations and spectral deconvolution studies;[11e−g] however, it follows closely the ordering first proposed by Gouterman and co-workers based on the SCMO-PPP-CI model.[13,14] The dotted line indicates the four orbitals referred to in Figure 2 that are based on Gouterman's original four-orbital LCAO model.[13] Interspersed with the π MOs of the inner perimeter cyclic polyene ring are MOs that are associated primarily with the peripheral portions of the extended π-system, Table 5. The lower orbitals on the right of the main $\pi \rightarrow \pi^*$ set are the four aza-nitrogen lone pair MOs. Transitions that give rise to *x*/*y*-polarized bands (and, therefore, A terms in the MCD spectrum) are represented with solid lines. Dashed lines are used for *z*-polarized transitions that are predicted to lie in the Q-band region and will give rise to MCD B terms. On the right-hand side, we show the states calculated to exhibit significant absorption intensity in the 250−1000 nm region, with the state symmetry for a D_{4h} molecular symmetry. The second $\pi \rightarrow \pi^*$ transition is observed as a very weak doubly degenerate band in the spectra of main group MPc(−2) complexes.

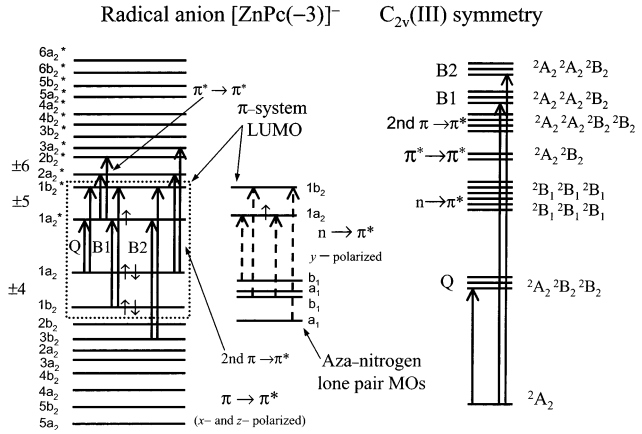

Figure 9. Molecular orbital and excited state energy level diagram of $[ZnPc(-3)]^-$ assuming C_{2v}(III) symmetry. The C_2 axis lies within the plane of the ring due to ring ruffling/doming when the aromaticity is lost through the addition of an extra electron to the π-system.[11c] The $n \rightarrow \pi^*$ transitions are placed between the Q_{vib} and B1 transitions on the basis of an earlier assignment of the Q-band region of $(CN^-)ZnPc(-2)$.[11d] The lowering of the symmetry results in all states being nondegenerate, for which the model predicts that there should only be B terms observed in the MCD spectrum. However, the B terms will occur as coupled pairs of opposite sign.

managers with respect to the number of atoms within the structure during geometry optimization calculations.

UV−visible absorption spectra were then calculated for $ZnF_{48}Pc(-2)$ and $[ZnF_{48}Pc(-3)]^-$ using the spectroscopic INDO Hamiltonian (INDO/s).[21,22] Since the spectrum predicted for $ZnF_{48}Pc(-2)$ is very similar to that of $ZnF_{64}Pc(-2)$, Tables 2 and 5, the ZINDO/s spectrum for $[ZnF_{48}Pc(-3)]^-$ can be

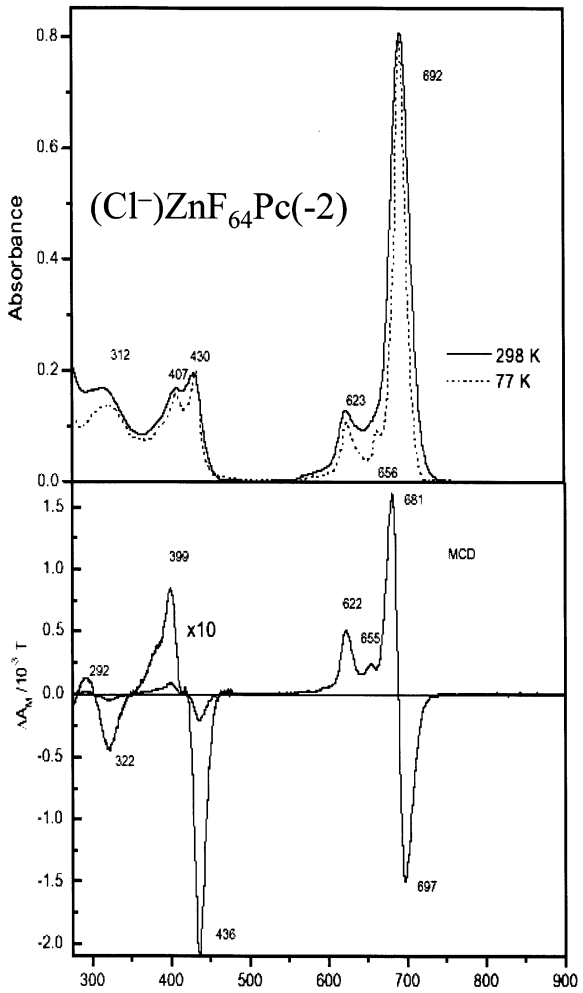

Figure 10. Electronic absorption (UV−visible) and MCD spectra of $(Cl^-)ZnF_{64}Pc(-2)$ in DMF at room temperature and in a 9:1 DMF/DMA vitrified mixture at 80 K (UV−visible) and 40 K (MCD).

expected to be very similar to the one that would have been obtained for $[ZnF_{64}Pc(-3)]^-$, if the geometry optimization had been possible. The ZINDO/s calculation was also carried out for 1,4,8,11,15,18,22,25-F-2,3,9,10,16,17,23,24-*i*-C_3F_7 ZnPc ($ZnF_{64}Pc(-2)$) based on the coordinates obtained from X-ray crystallography[10] in the absence of the acetone ligands and with an additional Cl^- ligand added to match the species studied during the spectroscopic measurements, Tables 5 and 6. When calculations were attempted for a $[(Cl^-)ZnF_{48}Pc(-3)]^-$ species in the absence of X-ray coordinates, the geometry optimization routines predicted a separation of the central metal and the Cl− axial ligand, which was sufficiently large that the resulting ZINDO/s spectrum was almost identical to that of $[ZnF_{48}Pc(-3)]^-$. The results of the ZINDO calculations for ZnPc(−2), $ZnF_{48}Pc(-2)$, $[ZnPc(-3)]^-$, $[ZnF_{48}Pc(-3)]^-$, $(Cl^-)ZnF_{64}Pc(-2)$, and $[(Cl^-)ZnF_{64}Pc(-3)]^-$ are shown in Tables 1−6, respectively. The energies of the π molecular orbitals (MOs) are tabulated in Tables 7−9 so that the one-electron transitions that are responsible for the bands in the ZINDO calculated spectra, Tables 1−6, can be readily compared despite the differences in orbital labeling due to differences in symmetry.

The distinctive nodal and antinodal patterns observed for the π-system MOs of ZnPc(−2) are also observed in the case of $ZnF_{48}Pc(-2)$, $ZnF_{64}Pc(-2)$, and $(Cl^-)ZnF_{64}Pc(-2)$. Figure 12

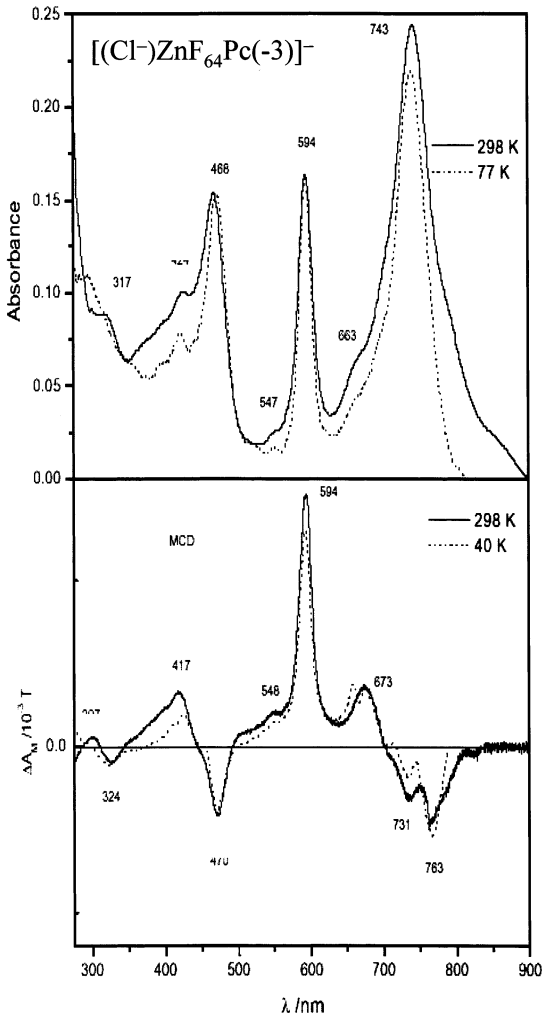

Figure 11. Electronic absorption (UV−visible) and MCD spectral data of $[ZnF_{64}Pc(-3)]^-$ in DMF at room temperature and in a 9:1 DMF/DMA vitrified mixture at 80 K (UV−visible) and 40 K (MCD). The anion radical was formed photochemically using hydrazine hydrate as the electron donor. No unreacted neutral species remains.

shows the nodal patterns calculated for six frontier π-system molecular orbitals of D_{4h} symmetry in ZnPc(−2) (top two rows) and C_{4h} symmetry in $ZnF_{64}Pc(-2)$ (bottom two rows) that are associated with the major $\pi \rightarrow \pi^*$ transitions in the UV−visible region, using data in Tables 1, 5, and 7. In Table 7, the orbitals have been ordered relative to the corresponding ZnPc(−2) MO so that the one-electron transitions that are responsible for the bands in the ZINDO calculated spectra, Tables 1−6, can be compared directly despite the symmetry-induced differences in orbital labeling. The results for the fluorinated phthalocyanines are assumed to be virtually independent of the presence or absence of axial acetone ligands. The X-ray structure of the bisacetone complex demonstrates that the solvent is not constrained within the fluorinated cavities and is, thus, unlikely to have any steric effect upon the geometry of the Pc ring.[10] Therefore, omission of the acetone from the calculation is not expected to result in ring distortions, a geometric change which would have influenced the outcome of the MO calculations. DFT geometry optimizations of the structures of ZnPc(−2), (Cl^-)ZnPc(−2), $[ZnPc(-3)]^-$, $ZnF_{16}Pc(-2)$, $[ZnF_{16}Pc(-3)]^-$, and $(Cl^-)ZnF_{16}Pc(-2)$ gave similar results to those obtained from the ZINDO/1 optimizations. Calculations for zinc tetraazaporphyrin (ZnTAP), ZnPc(−2), $[ZnPc(-1)]^+$, and $[ZnPc(-3)]^-$ have demonstrated that these techniques produce almost identical structures, most likely because for symmetric porphyrin and phthalocyanine ligands there is a planar heteroaromatic structure.[11g] These spectra can be compared to those reported previously for ZnPc(−2) and $[ZnPc(-3)]^-$ during the analysis of $[MPc(-(2+n))]^{n-}$ ($n = -1 \rightarrow 2$) species,[11d,g] Tables 1−4. Figure 13 shows the contours for the six frontier π-system molecular orbitals of C_{2v}(III) symmetry $[ZnPc(-3)]^-$ (top two rows) and $[ZnF_{48}Pc(-3)]^-$ (bottom two rows) species that are associated with the major $\pi \rightarrow \pi^*$ and $\pi^* \rightarrow \pi^*$ transitions in the UV−visible region, using data reported in Tables 3, 4, and 7.

Geometry optimization of a series of complexes substituted with −F, $-C_2F_5$, and i-C_3F_7 groups at the α-(1,4,8,11,15,18,22,25) and β-(2,3,9,10,16,17,23,24) positions were carried out using the CAChe MOPAC program[27] with PM3 parameters. Memory limitations made DFT optimizations of complexes with i-C_3F_7 groups at each of the eight α- or β-positions impossible. The optimized structures were used to calculate the UV−visible absorption spectra so that the λ_{max} values of the Q-band which arises from the lowest energy $\pi \rightarrow \pi^*$ transition could be compared, Figure 14. In this figure, the band maxima for each of the eight complexes are plotted. When the symmetry is lower than D_{4h}, the Q-band splits into two components.

Discussion

The substitution of protons in the ligand of the protio complex, $ZnH_{16}Pc(-2)$, by fluorine atoms and perfluoro alkyl groups has a profound effect upon its electronic structure, as reflected in changes of the electronic spectrum and redox potentials. These effects are particularly noticeable by the appearance of the ring-reduced, anion radical in the presence of oxygen in solutions. Such changes can be attributed, in principle, to molecular distortions or electronic effects or a combination of these two factors. Modeling the geometry using the CAChe MOPAC program for a series of complexes substituted with a combination of −F, $-C_2F_5$, and i-C_3F_7 groups at the α- and β-positions demonstrates that it is substitution at the α-position that has the greatest impact on the wavelength of the S1 excited state used in photodynamic therapy applications, Figure 14. Complexes with $-C_2F_5$ or i-C_3F_7 substituents at the α-position are predicted to be nonplanar due to the steric interactions between the alkyl groups. In contrast, at the β-position, the bulky i-C_3F_7 peripheral substituents do not alter either the Pc ring planarity or the central, in-plane position of the metal ion. The steric crowding resulting from their ortho position is relieved by their orientation such that the smaller tertiary fluorine atoms are almost in the plane of the Pc ring, while the bulky trifluoromethyl groups are above and below it, Figure 1.

Considering that (i) the ring planarity of $ZnF_{64}Pc(-2)$ is maintained in solid state[10] in the presence of axially coordinated acetone and that (ii) no unusual intermolecular interactions that might enforce ring planarity are revealed by the X-ray structure of $(acetone)_2ZnF_{64}Pc(-2)$, we find it is reasonable to assume that the Pc ring remains planar in solution. Thus, the observed spectroscopic effects of peripheral substitution of H by F and of F by i-C_3F_7 groups are primarily electronic in nature; that is,

(27) Stewart, J. J. P. *MOPAC 2002*; Fujitsu Limited: Tokyo, Japan, 1999.

Table 1. Calculated Electronic Excitation Spectrum of ZnPc(−2)

no.[a]	symmetry[b]	calcd[c]	obsd[d]	wave function[e]	assignment[f]
1	$^1A_{1g}$				ground state
2, 3	$^1E_{ux}$	14.8 (0.903)	14.8	$-0.950\|1e_g^*\leftarrow 1a_{1u}\rangle+0.260\|1e_g^*\leftarrow 1a_{2u}\rangle+...$	Q
6, 7	$^1E_{ux}$	30.0 (0.023)		$-0.978\|2e_g^*\leftarrow 1a_{1u}\rangle-0.073\|4e_g^*\leftarrow 1a_{1u}\rangle+...$	second $\pi\rightarrow\pi^*$
13	$^1A_{2u}$	34.1 (0.032)	16.5	$0.561\|1e_g^*\leftarrow e_u^N\rangle-0.472\|1b_{2u}^*\leftarrow b_{1g}^N\rangle+...$	$n\rightarrow\pi^*$
14, 15	$^1E_{ux}$	34.3 (0.428)	25.5	$0.808\|1e_g^*\leftarrow 1b_{1u}\rangle-0.255\|1b_{2u}^*\leftarrow 1e_g\rangle$ $-0.221\|1e_g^*\leftarrow 1a_{2u}\rangle+...$	B1
16, 17	$^1E_{ux}$	34.7 (2.233)	29.9	$-0.815\|1e_g^*\leftarrow 1a_{2u}\rangle-0.348\|3e_g^*\leftarrow 1a_{1u}\rangle$ $-0.252\|1e_g^*\leftarrow 1b_{1u}\rangle+0.228\|1e_g^*\leftarrow 1a_{1u}\rangle+...$	B2
21, 22	$^1E_{ux}$	36.5 (0.330)	33.6	$-0.574\|3e_g^*\leftarrow 1a_{1u}\rangle+0.371\|1e_g^*\leftarrow 1a_{2u}\rangle$ $-0.259\|1b_{1u}^*\leftarrow 1e_g\rangle-0.251\|2e_g^*\leftarrow 2a_{2u}\rangle$ $-0.222\|2e_g^*\leftarrow 1b_{1u}\rangle+...$	N
29, 31	$^1E_{ux}$	39.0 (0.014)	36.2	$-0.635\|3e_g^*\leftarrow 1a_{1u}\rangle-0.593\|1e_g^*\leftarrow 2b_{2u}\rangle$ $+0.278\|1e_g^*\leftarrow 2a_{1u}\rangle+0.216\|1b_{2u}\leftarrow 2e_g^*\rangle+...$	L
34, 35	$^1E_{ux}$	41.1 (0.019)	40.7	$-0.744\|1e_g^*\leftarrow 1b_{2u}\rangle+0.451\|1e_g^*\leftarrow 1b_{1u}\rangle$ $-0.293\|1e_g^*\leftarrow 2a_{2u}\rangle+0.255\|3e_g^*\leftarrow 1a_{1u}\rangle+...$	C

[a] The number of the state assigned in terms of ascending energy in the ZINDO calculation. Only states that result from allowed electronic transitions with a nonzero oscillator strength are included in the table. [b] The symmetry of the state under D_{4h} symmetry. [c] The calculated band energies (10^3 cm^{-1}) and oscillator strengths in parentheses. [d] Observed energies (10^3 cm^{-1}) from the data of Nyokong et al.[11a] [e] The calculated wave functions based on the eigenvectors produced by the configuration interaction calculation of the ZINDO program. N denotes orbitals associated with the aza-nitrogen lone pair orbitals. The orbital energies are shown in Tables 7 and 8. [f] The assignment is described in the text.

Table 2. Calculated Electronic Excitation Spectrum of $ZnF_{48}Pc(-2)$

no.[a]	symmetry[b]	calcd[c]	obsd[d]	wave function[e]	assignment[f]
1	^1A_g				ground state
2, 3	$^1E_{ux}$	14.4 (1.104)	14.5	$-0.982\|1e_g^*\leftarrow 1a_u\rangle+...$	Q
6, 7	$^1E_{ux}$	28.2 (0.047)		$-0.602\|2e_g^*\leftarrow 1a_u\rangle^A+0.326\|2e^*\leftarrow 1a_u\rangle^B$ $-0.270\|2e_g^*\leftarrow 1b_u\rangle+...$	second $\pi\rightarrow\pi^*$
10, 11	$^1E_{ux}$	32.9 (1.402)	23.3	$0.690\|1e_g^*\leftarrow 2a_u\rangle-0.443\|2e_g^*\leftarrow 1a_u\rangle+...$	B1
18, 19	$^1E_{ux}$	34.4 (0.555)	25.0	$0.438\|3e_g^*\leftarrow 1a_u\rangle-0.295\|1e_g^*\leftarrow 2e_g\rangle$ $-0.289\|1e_g^*\leftarrow 2b_u\rangle+...$	B2
20	^1A_u	35.5 (0.021)		$-0.753\|a_g^\sigma\leftarrow 1a_u\rangle+0.239\|1e_g^*\leftarrow 1e_u^N\rangle+...$	$\pi\rightarrow\sigma^*/n\rightarrow\pi^*$
23, 24	$^1E_{ux}$	36.0 (0.836)		$0.457\|2e_g^*\leftarrow 1a_u\rangle^A+0.435\|1e_g^*\leftarrow 1b_2\rangle$ $+0.291\|3e_g^*\leftarrow 1a_u\rangle+0.266\|2e_g^*\leftarrow 1a_u\rangle^B$ $+0.216\|2b_u\leftarrow 2e_g^*\rangle+...$	

[a] The number of the state assigned in terms of ascending energy in the ZINDO calculation. Only states that result from allowed electronic transitions with a nonzero oscillator strength below 36 000 cm^{-1} are included in the table. [b] The symmetry of the state under C_{4h} symmetry. [c] The calculated band energies (10^3 cm^{-1}) and oscillator strengths in parentheses. [d] Observed energies (10^3 cm^{-1}). [e] The calculated wave functions based on the eigenvectors produced by the configuration interaction calculation of the ZINDO program. N denotes orbitals associated with the aza-nitrogen lone pair orbitals. σ denotes a σ orbital associated with the peripheral fluorines. The orbital energies of the π MOs are shown in Tables 7 and 8. [f] The assignment is described in the text.

they are due to the electronic withdrawing effect of the fluorinated groups rather than to their bulkiness. It is interesting to note that the combination of F and *i*-C_3F_7 substituents in $ZnF_{64}Pc(-2)$ is more electron withdrawing not only in comparison with $ZnH_{16}Pc(-2)$ but also in comparison with ZnF_{16}-Pc(−2).[10] The decrease in electron density of the Pc ring upon the substitution of aromatic F in $ZnF_{16}Pc(-2)$ by *i*-C_3F_7 groups has been attributed to loss of aromatic fluorine conjugation.[10] Thus, the metallo-macrocycle ring moiety of $ZnF_{64}Pc(-2)$ is expected to be extremely electron deficient and to resist oxidation while favoring the addition of electrons to form anions, as observed electrochemically and photochemically. Notably, octanitro[12] and cyano[28] have redox couples of the order +900 mV from unsubstituted phthalocyanines, but there are residual C−H groups present in these compounds and the chemical (as opposed to electrochemical) resistance to oxidation is problematic. Their aggregation in solution and the absence of axial Cl^- ligation are additional differences relative to the molecules described in this work.

Optical Spectra of $ZnF_{64}Pc(-2)$. In its simplest description, the optical spectroscopy of MPc(−2) can be accounted for by considering only the 16-atom, 18-π-electron cyclic polyene aromatic system that runs around the inner perimeter of the Pc ligand, Figure 15. Gouterman's model of this inner cyclic polyene, based on a four-orbital linear combination of atomic orbitals (LCAO), has been widely used to describe the optical spectra of both MPor(−2) (Por = porphyrin) and MPc(−2) complexes.[12,13] In this model, illustrated in Figures 2, 8, and 9, the HOMO has an M_L value of±4, while the LUMO has an M_L value of ±5. The association of orbital angular momentum (OAM) with pairs of orbitals follows from the assignment of the molecular orbitals of the aromatic ring system in terms of the OAM associated with the complex wave functions of an ideal cyclic polyene in the sequence 0, ±1, ±2,.., ±7, 8 based on their nodal and antinodal patterns. In this simple scheme, there are four transitions between the HOMO and the LUMO levels involving changes in orbital angular momentum of $\Delta M_L = \pm 1$ and ±9, Figures 2 and 8, referred to as the B and Q transitions, respectively. In the case of porphyrins, these transitions are forbidden and, thus, weak. The addition of the aza-linkages and peripheral fused benzene rings, that is, the case of MPc(−2), breaks the degeneracy of the HOMO level significantly so that the $1a_{1u}$ and $1a_{2u}$ orbitals become widely separated. Consequently, the Q and B band sets are observed near 670 and 300 nm, respectively. Furthermore, as a consequence of the loss of HOMO degeneracy, and with $1a_{1u}$ lying

(28) (28) Giraudeau, A.; Louati, A.; Gross, M.; Andre, J. J.; Simon, J.; Su, C. H.; Kadish, K. M. *J. Am. Chem. Soc.* **1983**, *105*, 2917.

Table 3. Calculated Electronic Excitation Spectrum of $[ZnPc(-3)]^-$

no.[a]	symmetry[b]	calcd[c]	obsd[d]	wave function[e]	assignment[f]
1	$^2A_2$				ground state
3	$^2A_2$	8.87 (0.097)	10.4	$0.842\|1a_2^*\leftarrow 1a_2\rangle + 0.370\|2a_2^*\leftarrow 2a_2\rangle - 0.281\|2a_2^*\leftarrow 1a_2\rangle^B + ...$	Q_z
4	$^2B_2$	10.4 (0.069)	10.8	$-0.683\|1b_2^*\leftarrow 1a_2\rangle^B + 0.438\|1b_2^*\leftarrow 1a_2\rangle^A - 0.435\|2b_2^*\leftarrow 2a_2^*\rangle + ...$	Q_x
5	$^2A_2$	16.6 (0.594)	15.7	$0.797\|2a_2^*\leftarrow 1a_2^*\rangle - 0.356\|1a_2^*\leftarrow 1a_2\rangle + 0.238\|1b_2^*\leftarrow 1b_2\rangle + ...$	$\pi^* \rightarrow \pi^*_z$
6	$^2B_2$	17.0 (0.292)	11.4	$-0.665\|3b_2^*\leftarrow 1a_2^*\rangle - 0.423\|2b_2^*\leftarrow 1a_2^*\rangle - 0.380\|1b_2^*\leftarrow 1a_2\rangle^A + ...$	$\pi^* \rightarrow \pi^*_x$
7	$^2B_2$	18.9 (0.469)	17.5	$-0.508\|1b_2^*\leftarrow 1a_2\rangle^A + 0.434\|4b_2^*\leftarrow 1a_2\rangle^B - 0.448\|4b_2^*\leftarrow 1a_2^*\rangle + 0.257\|3b_2^*\leftarrow 1a_2^*\rangle - 0.235\|2b_2^*\leftarrow 1a_2^*\rangle + 0.209\|2b_2^*\leftarrow 1a_2\rangle^B + ...$	Q_x/second $\pi^* \rightarrow \pi^*_x$
8	$^2B_2$	21.5 (0.207)		$-0.419\|1b_2^*\leftarrow 1a_2\rangle^A - 0.325\|1b_2^*\leftarrow 1a_2\rangle^B - 0.420\|4b_2^*\leftarrow 1a_2\rangle^B + 0.298\|3b_2^*\leftarrow 1a_2^*\rangle + 0.226\|6b_2^*\leftarrow 1a_2^*\rangle + ...$	Q_x/second $\pi^* \rightarrow \pi^*_x$
13	$^2A_2$	25.6 (0.130)		$-0.564\|4a_2^*\leftarrow 1a_2^*\rangle - 0.512\|4a_2^*\leftarrow 1a_2\rangle^A - 0.361\|3a_2^*\leftarrow 1a_2^*\rangle - 0.200\|6a_2^*\leftarrow 1a_2^*\rangle + ...$	second $\pi^* \rightarrow \pi^*_z$
14	$^2B_2$	26.0 (0.179)	23.0	$-0.631\|1a_2^*\leftarrow 3b_2\rangle + 0.380\|1a_2^*\leftarrow 2b_2\rangle + 0.366\|1a_2^*\leftarrow 1b_2\rangle + ...$	$B1/B2_x$
17	$^2B_2$	27.3 (0.124)	24.8	$0.631\|4b_2^*\leftarrow 1a_2\rangle^A - 0.216\|4b_2^*\leftarrow 1a_2\rangle^B + 0.314\|1a_2^*\leftarrow 1b_2\rangle + 0.305\|4b_2^*\leftarrow 1a_2^*\rangle - 0.252\|1a_2^*\leftarrow 2b_2\rangle - 0.212\|1a_2^*\leftarrow 1b_2\rangle + ...$	second $\pi \rightarrow \pi^*_x$
19	$^2B_2$	28.3 (0.173)		$0.528\|4b_2^*\leftarrow 1a_2\rangle^A - 0.204\|4b_2^*\leftarrow 1a_2\rangle^B - 0.438\|1a_2^*\leftarrow 1b_2\rangle + 0.249\|2a_2^*\leftarrow 1b_2\rangle + 0.240\|1a_2^*\leftarrow 2b_2\rangle + ...$	second $\pi \rightarrow \pi^*_x$
23	$^2B_2$	30.8 (0.486)		$-0.400\|3b_2^*\leftarrow 1a_2\rangle^A + 0.258\|3b_2^*\leftarrow 1a_2\rangle^B - 0.304\|2a_2^*\leftarrow 1a_2\rangle^A + 0.327\|1a_2^*\leftarrow 3b_2\rangle + 0.305\|1a_2^*\leftarrow 2b_2\rangle - 0.292\|1a_2^*\leftarrow 5b_2\rangle + 0.219\|1a_2^*\leftarrow 1b_2\rangle + ...$	$B1/B2_x$
25	$^2B_2$	31.9 (0.255)		$0.686\|3b_2^*\leftarrow 1a_2\rangle^A + 0.262\|1a_2^*\leftarrow 1b_2\rangle - 0.205\|6b_2^*\leftarrow 1a_2^*\rangle - 0.202\|5b_2^*\leftarrow 1a_2^*\rangle^B + ...$	$B1/B2_x$
27	$^2B_2$	32.6 (0.141)		$0.293\|2b_2^*\leftarrow 1a_2\rangle^B + 0.245\|1a_2^*\leftarrow 1b_2\rangle - 0.263\|3b_2^*\leftarrow 1a_2\rangle + 0.255\|6b_2^*\leftarrow 1a_2\rangle - 0.259\|3a_2^*\leftarrow 4b_2\rangle^B - 0.223\|1b_2^*\leftarrow 3a_2\rangle^B + ...$	
31	$^2A_2$	34.0 (0.274)		$-0.578\|1b_2^*\leftarrow 1b_2\rangle^B + 0.187\|1b_2^*\leftarrow 2b_2\rangle^A - 0.265\|4b_2^*\leftarrow 2b_2\rangle^B + 0.222\|3a_2^*\leftarrow 1a_2\rangle^A - 0.219\|3a_2^*\leftarrow 1a_2\rangle^B - 0.222\|5a_2^*\leftarrow 1a_2\rangle^A + ...$	$B1/B2_z$
34	$^2A_2$	34.8 (0.115)		$0.370\|1a_2^*\leftarrow 3a_2\rangle + 0.338\|5a_2^*\leftarrow 1a_2\rangle^A + 0.272\|1b_2^*\leftarrow 1b_2\rangle^A - 0.282\|2a_2^*\leftarrow 1a_2\rangle^A + ...$	
36	$^2A_2$	35.1 (0.352)		$-0.473\|5a_2^*\leftarrow 1a_2\rangle^A + 0.227\|1b_2^*\leftarrow 1b_2\rangle^A + 0.291\|1b_2^*\leftarrow 2b_2\rangle^A + ...$	

[a] The number of the state assigned in terms of ascending energy in the ZINDO calculation. Only states that result from allowed electronic transitions with a calculated oscillator strength greater than 0.1 are included in the table. [b] The symmetry of the state under C_{2v}(III) symmetry. [c] The calculated band energies (10^3 cm^{-1}) and oscillator strengths in parentheses. [d] Observed band energies (10^3 cm^{-1}) from the data of Mack and Stillman.[11c] [e] The calculated wave functions based on the eigenvectors produced by the configuration interaction calculation of the ZINDO program. A and B refer to separate spin-allowed excited state configurations associated with one-electron transitions linking the same orbitals. N denotes orbitals associated with the aza-nitrogen lone pair orbitals. The orbital energies are shown in Table 9. [f] The assignment is described in the text.

significantly above $1a_{2u}$, the mixing between the Q and B excited states is much reduced, and the Q-band gains significantly in intensity. The spectral deconvolution studies of phthalocyanines[11,17] have indicated that there are in fact two separate A terms of almost equal magnitude and bandwidth in the B band region of the porphyrins (250−400 nm). These B1 and B2 bands can only be resolved clearly in the presence of certain axial ligands, such as CN^-. The band assignment sequence has, therefore, been modified to include separate B1 and B2 transitions superimposed in the 350 nm region,[11a,g] Figure 8.

We have used Gouterman's MO models to assign the Q, B or B1/B2, N, L, and C bands observed in the optical spectra of a variety of metalloporphyrins, MPor(−2), and MPc(−2) complexes and their cation and anion radical species, based on spectral deconvolution of the UV−visible absorption and magnetic circular dichroism (MCD) spectroscopy[11,15] by means of the SIMPFIT program.[16] A number of more recent MO calculations for MPc complexes have been reported,[18] but Gouterman's four-orbital model still provides a good starting framework for describing the MCD spectroscopy of both porphyrin and phthalocyanine complexes.

Spectral Deconvolution Identifies the Major Contributing Bands in the Spectrum. The ground states of divalent, main group metal MPc(−2) complexes are nondegenerate, $^1A_{1g}$, under D_{4h} symmetry, so there are no Faraday C terms in the MCD spectrum and the observed MCD spectrum at low shaped A terms locates the major electronic bands, Figure 16. Although the symmetry of the nodal patterns of the MOs of the π-systems of $ZnF_{48}Pc(-2)$, $ZnF_{64}Pc(-2)$, and $(Cl^-)ZnF_{64}Pc(-2)$ predicted by the INDO/1 calculations are reduced to C_{4h}, the same *x*/*y*-polarized $\pi \rightarrow \pi^*$ transitions linking ^1A_g ground states and ^1E_u excited states are responsible for the major bands within the optical spectra, Tables 1−6. For comparison purposes, the spectrum of $(CN^-)ZnPc(-2)$ will be considered here first.[11d] As with the perfluoroZnPc, the spectral data are for the (X^-) axially bound Zn(II). The low temperature absorption and MCD spectra closely resemble those recorded at room temperature (Figure 10). The $\pi \rightarrow \pi^*$ transitions to ^1E_u excited states are

Table 4. Calculated Electronic Excitation Spectrum of $[ZnF_{48}Pc(-3)]^-$

no.[a]	symmetry[b]	calcd[c]	obsd[d]	wave function[e]	assignment[f]
1	^2A				ground state
3	^2A	8.56 (0.063)	13.5	$-0.828\|1a^*\leftarrow 1a\rangle - 0.429\|2a^*\leftarrow 2a\rangle + ...$	Q_z
4	^2B	11.7 (0.130)	14.3	$-0.661\|1b^*\leftarrow 1a\rangle^B + 0.471\|1b^*\leftarrow 1a\rangle^A + 0.421\|2b^*\leftarrow 1a^*\rangle + ...$	Q_x
5	^2A	15.6 (0.715)	12.9	$0.775\|2a^*\leftarrow 1a^*\rangle - 0.400\|1a^*\leftarrow 1a\rangle + ...$	$\pi^* \rightarrow \pi^*_z$
6	^2B	16.3 (0.371)	15.4	$-0.676\|3b^*\leftarrow 1a^*\rangle - 0.436\|1b^*\leftarrow 1a\rangle^A + 0.351\|2b^*\leftarrow 1a^*\rangle + ...$	Q_x/second $\pi^* \rightarrow \pi^*_x$
7	^2B	18.0 (0.337)		$-0.520\|4b^*\leftarrow 1a^*\rangle - 0.475\|4b^*\leftarrow 1a\rangle^B - 0.399\|1b^*\leftarrow 1a\rangle^A + 0.278\|3b^*\leftarrow 1a^*\rangle^B + ...$	Q_x/second $\pi^* \rightarrow \pi^*_x$
9	^2B	21.5 (0.236)	16.8	$-0.454\|2b^*\leftarrow 1a^*\rangle - 0.438\|4b^*\leftarrow 1a^*\rangle - 0.365\|3b^*\leftarrow 1a\rangle + 0.365\|1b^*\leftarrow 1a\rangle^A + 0.310\|1b^*\leftarrow 1a^*\rangle^B + 0.284\|4b^*\leftarrow 1a^*\rangle^B + ...$	$\pi^* \rightarrow \pi^*_x$
12	^2A	24.0 (0.096)		$0.738\|4a^*\leftarrow 1a\rangle^A - 0.392\|4a^*\leftarrow 1a^*\rangle + 0.288\|3a^*\leftarrow 1a^*\rangle + ...$	second $\pi^* \rightarrow \pi^*_z$
15	^2B	26.0 (0.282)		$-0.613\|4b^*\leftarrow 1a\rangle^A - 0.405\|1b^*\leftarrow 1b\rangle + 0.264\|4b^*\leftarrow 1a\rangle^B + ...$	$B1/B2_x$
16	^2A	26.1 (0.103)		$0.527\|3a^*\leftarrow 1a\rangle^A - 0.360\|3a^*\leftarrow 1a\rangle^B - 0.304\|5a^*\leftarrow 1a + ...$	second $\pi \rightarrow \pi^*_z$
17	^2B	26.4 (0.089)		$-0.494\|1a^*\leftarrow 3b\rangle + 0.454\|4b^*\leftarrow 1a\rangle^A - 0.339\|1a^*\leftarrow 2b\rangle - 0.276\|1a^*\leftarrow 1b\rangle + ...$	
19	^2B	27.9 (0.361)	21.1	$0.483\|1a^*\leftarrow 2b\rangle - 0.468\|1a^*\leftarrow 1b\rangle + ...$	$B1/B2_x$
23	^2B	29.7 (0.249)		$0.528\|3b^*\leftarrow 1a\rangle^A + 0.428\|1a^*\leftarrow 3b\rangle - 0.317\|1a^*\leftarrow 2b\rangle + 0.284\|2a^*\leftarrow 2b\rangle - 0.257\|1a^*\leftarrow 1b\rangle + ...$	second $\pi^* \rightarrow \pi^*_x$
24	^2B	30.0 (0.157)		$-0.621\|3b^*\leftarrow 1a\rangle^A - 0.285\|1a^*\leftarrow 2b\rangle - 0.280\|1a^*\leftarrow 1b\rangle + ...$	$B1/B2_x$
28	^2B	31.8 (0.140)		$0.394\|5b^*\leftarrow 1a\rangle^B - 0.367\|5b^*\leftarrow 1a\rangle^A + 0.327\|1a^*\leftarrow 5a\rangle^B - 0.272\|2a^*\leftarrow 4b\rangle^B - 0.256\|1a^*\leftarrow 1b\rangle + ...$	
30	^2A	32.9 (0.414)		$0.392\|1a^*\leftarrow 4a\rangle + 0.356\|5a^*\leftarrow 1a\rangle^A + 0.327\|1a^*\leftarrow 5a\rangle^B + 0.311\|1b^*\leftarrow 1b\rangle^B - 0.231\|1b^*\leftarrow 1b\rangle^A + ...$	
33	^2A	33.1 (0.339)	23.3	$-0.387\|1b^*\leftarrow 1b\rangle^A + 0.242\|1b^*\leftarrow 1b\rangle^B - 0.371\|4a^*\leftarrow 1a\rangle^A - 0.257\|1b^*\leftarrow 4b\rangle^B - 0.257\|1a^*\leftarrow 4a\rangle^B + ...$	$B1/B2_z$
35	^2A	34.3 (0.098)		$-0.309\|1b^*\leftarrow 1b\rangle^B - 0.275\|4b^*\leftarrow 2b\rangle^B + 0.263\|4a^*\leftarrow 1a\rangle^A + 0.263\|6a^*\leftarrow 1a^*\rangle - 0.259\|2a^*\leftarrow 1a\rangle^B + ...$	

[a] The number of the state assigned in terms of ascending energy in the ZINDO calculation. Only states that result from allowed electronic transitions with a calculated oscillator strength greater than 0.1 are included in the table. [b] The symmetry of the state under C_2 symmetry. [c] The calculated band energies (10^3 cm^{-1}) and oscillator strengths in parentheses. [d] Observed band energies (10^3 cm^{-1}). [e] The calculated wave functions based on the eigenvectors produced by the configuration interaction calculation of the ZINDO program. A and B refer to separate spin-allowed excited state configurations associated with one-electron transitions linking the same orbitals. N denotes orbitals associated with the aza-nitrogen lone pair orbitals. The orbital energies are shown in Table 9. [f] The assignment is described in the text.

Table 5. Calculated Electronic Excitation Spectrum of $ZnF_{64}Pc(-2)$

no.[a]	symmetry[b]	calcd[c]	obsd[d]	wave function[e]	assignment[f]
1	^1A_g				ground state
2, 3	$^1E_{ux}$	14.7 (1.013)	14.5	$-0.952\|1e_g^*\leftarrow 1a_u\rangle + 0.251\|1e_g^*\leftarrow 2a_u\rangle ...$	Q
6, 7	$^1E_{ux}$	28.3 (0.062)		$-0.977\|2e_g^*\leftarrow 1a_u\rangle + ...$	second $\pi \rightarrow \pi^*$
10, 11	$^1E_{ux}$	32.7 (0.801)	23.3	$0.723\|3e_g^*\leftarrow 1a_u\rangle - 0.424\|1e_g^*\leftarrow 2a_u\rangle + 0.207\|1e_g^*\leftarrow 1b_u\rangle + ...$	B1
18, 19	$^1E_{ux}$	34.8 (0.388)		$0.504\|1e_g^*\leftarrow 1b_u\rangle - 0.467\|1e_g^*\leftarrow 2b_u\rangle + 0.303\|1e_g^*\leftarrow 3a_u\rangle + 0.282\|1e_g^*\leftarrow 2b_u\rangle + 0.273\|1e_g^*\leftarrow 1a_u\rangle - 0.201\|1b_u^*\leftarrow 1e_g\rangle + ...$	B2
20, 21	$^1E_{ux}$	35.7 (0.444)		$0.551\|3e_g^*\leftarrow 1a_u\rangle - 0.414\|1e_g^*\leftarrow 1b_u\rangle + 0.340\|1e_g^*\leftarrow 2b_u\rangle + 0.265\|1e_g^*\leftarrow 2a_u\rangle + ...$	
23, 24	$^1E_{ux}$	36.3 (1.198)		$-0.474\|1e_g^*\leftarrow 2a_u\rangle - 0.425\|3e_g^*\leftarrow 1a_u\rangle^A + 0.228\|1e_g^*\leftarrow 3a_u\rangle + 0.204\|3e_g^*\leftarrow 1a_u\rangle^B + 0.204\|1b_u\leftarrow 2e_g^*\rangle + ...$	

[a] The number of the state assigned in terms of ascending energy in the ZINDO calculation. Only states that result from allowed electronic transitions with a nonzero oscillator strength below 36 000 cm^{-1} are included in the table. [b] The symmetry of the state under C_{4h} symmetry. [c] The calculated band energies (10^3 cm^{-1}) and oscillator strengths in parentheses. [d] Observed energies (10^3 cm^{-1}). [e] The calculated wave functions based on the eigenvectors produced by the configuration interaction calculation of the ZINDO program. The orbital energies are shown in Tables 7 and 8. [f] The assignment is described in the text.

fully allowed with *x*/*y* polarization, Table 1, while *z*-polarized transitions to vibronic and nπ^* excited states with $^1A_{2u}$ are also possible. The energies of the $(CN^-)ZnPc(-2)$ vibrational bands are in good agreement with those reported in the Shpol'skii matrix emission studies of Huang et al.,[29] where much narrower bandwidths were obtained. Huang et al. proposed that there is a *z*-polarized n $\rightarrow$ π^* band at 604 nm with the aza-nitrogen lone pair orbitals at slightly higher energy than the Q transition

Table 6. Calculated Electronic Excitation Spectrum of $(Cl^-)ZnF_{64}Pc(-2)$

no.[a]	symmetry[b]	calcd[c]	obsd[d]	wave function[e]	assignment[f]
1	$^1A_1$				ground state
2, 3	^1E_x	14.3 (0.838)	14.5	$-0.902\|1e^*\leftarrow 1a\rangle + ...$	Q
5, 6	^1E_x	23.8 (0.794)	23.3	$-0.854\|1e^*\leftarrow 2a\rangle^A - 0.310\|1e^*\leftarrow 1a\rangle + 0.261\|1e^*\leftarrow 2a\rangle^B + ...$	B1
10, 12	^1E_x	26.2 (0.035)	25.0	$-0.973\|2e^*\leftarrow 1a\rangle + ...$	second $\pi \rightarrow \pi^*$
16, 17	^1E_x	32.0 (0.031)		$0.582\|2e^*\leftarrow 1a\rangle - 0.546\|\sigma^*\leftarrow 1a\rangle - 0.304\|\sigma^*\leftarrow 1a\rangle + 0.221\|3e^*\leftarrow 1a\rangle + ...$	
30	$^1A_1$	35.3 (0.019)		$-0.626\|1e^*\leftarrow 3e^N\rangle^A + 0.507\|1e^*\leftarrow 3e^N\rangle^B + 0.431\|1b^*\leftarrow 1b^N\rangle - 0.219\|3b^*\leftarrow 1b^N\rangle + ...$	$n \rightarrow \pi^*$
31, 32	^1E_x	35.7 (0.044)		$-0.439\|1e^*\leftarrow 1b\rangle + 0.383\|1e^*\leftarrow 2b\rangle - 0.254\|1e^*\leftarrow 4a\rangle + 0.241\|3e^*\leftarrow 1a\rangle + 0.220\|1b^*\leftarrow 1e\rangle^A + 0.211\|1b^*\leftarrow 1e\rangle^B + ...$	

[a] The number of the state assigned in terms of ascending energy in the ZINDO calculation. Only states that result from allowed electronic transitions with a nonzero oscillator strength below 36 000 cm^{-1} are included in the table. [b] The symmetry of the state under C_4 symmetry. [c] The calculated band energies (10^3 cm^{-1}) and oscillator strengths in parentheses. [d] Observed energies (10^3 cm^{-1}). [e] The calculated wave functions based on the eigenvectors produced by the configuration interaction calculation of the ZINDO program. N denotes orbitals associated with the aza-nitrogen lone pair orbitals. The orbital energies are shown in Tables 7 and 8. [f] The assignment is described in the text.

Table 7. Energies of the π-System MOs of ZnPc(−2), $ZnF_{48}Pc(-2)$, $ZnF_{64}Pc(-2)$, and $(Cl^-)ZnF_{64}Pc(-2)$[a]

	π MO	ZnPc(−2)	π MO	$ZnF_{48}Pc(-2)$	π MO	$ZnF_{64}Pc(-2)$	π MO	$(Cl^-)ZnF_{64}Pc(-2)$
M_L	D_{4h}	eV	C_{4h}	eV	C_{4h}	eV	C_4	eV
8	$2a_{2u}$*	2.961	$3a_u$*	1.780	$3a_u$*	1.843	3a*	4.795
±7	$4e_g$*	2.945	$4e_g$*	1.587	$4e_g$*	1.636	4e*	4.066
		2.946		1.584		1.628		4.047
	$2b_{2u}$*	2.31	$4b_u$*	0.739	$4b_u$*	0.767	4b*	3.414
	$2b_{1u}$*	2.066	$3b_u$*	0.734	$3b_u$*	0.736	3b*	3.059
	$3e_g$*	1.677	$3e_g$*	0.029	$3e_g$*	0.068	3e*	2.162
		1.676		0.017		0.102		2.132
	$1a_{1u}$*	1.544	$2a_u$*	−0.193	$2a_u$*	−0.318	2a*	1.872
	$1a_{2u}$*	0.787	$1a_u$*	−0.701	$1a_u$*	−0.626	1a*	1.633
	$2e_g$*	0.736	$2e_g$*	−0.775	$2e_g$*	−0.703	2e*	1.553
		0.734		−0.782		−0.724		1.532
±6	$1b_{2u}$*	0.359	$2b_u$*	−1.066	$2b_u$*	−0.950	2b*	1.408
	$1b_{1u}$*	0.098	$1b_u$*	−1.421	$1b_u$*	−1.367	1b*	0.928
±5	$1e_g$*	−1.495	$1e_g$*	−2.824	$1e_g$*	−2.728	1e*	−0.182
		−1.493		−2.829		−2.739		−0.192
±4	$1a_{1u}$	−5.534	$1a_u$	−6.784	$1a_u$	−6.752	1a	−4.227
	$1a_{2u}$	−8.318	$2a_u$	−9.558	$2a_u$	−9.584	2a	−5.960
	$1b_{1u}$	−8.78	$2b_u$	−10.135	$2b_u$	−10.075	2b	−7.807
	$1e_g$	−8.811	$1e_g$	−9.881	$1e_g$	−9.916	1e	−7.570
		−8.813		−9.884		−9.928		−7.595
	$2e_g$	−9.021	$2e_g$	−10.163	$2e_g$	−10.082	2e	−7.791
		−9.021		−10.177		−10.090		−7.818
	$2a_{2u}$	−9.161	$4a_u$	−10.565	$3a_u$	−10.392	3a	−7.398
	$1b_{2u}$	−9.297	$1b_u$	−9.962	$1b_u$	−9.979	1b	−7.652
	$2a_{1u}$	−9.711	$3a_u$	−10.508	$4a_u$	−10.501	4a	−8.229
±3	$3e_g$	−10.695	$3e_g$	−11.754	$3e_g$	−11.744	4e	−9.165
		−10.698		−11.761		−11.767		−9.196
	$3a_{2u}$	−13.292	$5a_u$	−13.967	$5a_u$	−14.294	5a[b]	−8.330

[a] The orbitals of $ZnF_{48}Pc(-2)$, $ZnF_{64}Pc(-2)$, and $(Cl^-)ZnF_{64}Pc(-2)$ are ordered in terms of the energies of the corresponding ZnPc(−2) orbital which shows the same pattern of nodes and antinodes in electron density to facilitate comparison of the calculated optical spectra of D_{4h}, C_{4h}, and C_4 complexes. The orbital angular momentums associated with the orbitals located primarily on the inner cyclic polyene are shown in the left-hand column. [b] The 5a MO of $(Cl^-)ZnF_{64}Pc(-2)$ is destabilized due to the presence of the (X^-) axial ligand.

which gives rise to a second set of weak vibrational bands to the blue of the Q transition, since the fluorescence excitation and emission spectra did not have the anticipated mirror symmetry. The results of the spectral band deconvolution of $(CN^-)ZnPc(-2)$ were consistent with the presence of this weak *z*-polarized $n \rightarrow \pi^*$ band.[11d] In contrast, most recent MO calculations[18] predict that the $n \rightarrow \pi^*$ transition occurs at a much higher energy, Table 1. For $ZnF_{64}Pc(-2)$, the deconvolution of the vibrational components, Q_{vib}, to the blue of the main Q_{00} band, Figure 16, requires far fewer bands, but the individual vibrational bands could not be resolved because of the low resolution. The presence of an $n \rightarrow \pi^*$ band as the origin of the second weaker set of vibrational bands observed between 550 and 610 nm, while possible, cannot be confirmed.[11d] Further light on the electronic structures of perfluoroalkyl phthalocyanines is shed by ZINDO calculations. The data in Table 1 indicate that the splitting of the $1a_{1u}$ and $1a_{2u}$ HOMOs of MPc(−2) is of sufficient magnitude for the $1a_{1u} \rightarrow 2e_g$* transition to occur at a lower energy than that of the allowed $1a_{2u} \rightarrow 1e_g$* B1 transition, Figure 8. A very weak, derivative-shaped signal at around 435 nm present in the MCD spectrum of MgPc(−2)[11e,g,17b] was previously assigned as an A term associated with this second $\pi \rightarrow \pi^*$ transition that was not part of the original Gouterman band assignment scheme, Figure 8.

(29) (a) Huang, T. H.; Reickhoff, K. E.; Voigt, E. M. *J. Chem. Phys.* **1982**, *77*, 3424. (b) Huang, T. H.; Reickhoff, K. E.; Voigt, E. M. *J. Phys. Chem.* **1981**, *85*, 3322.

Table 8. Calculated Energies and Symmetries of the σ MOs of ZnPc(−2), $ZnF_{48}Pc(-2)$, $ZnF_{64}Pc(-2)$, $(Cl^-)ZnF_{64}Pc(-2)$, $[ZnPc(-3)]^-$, and $[ZnF_{48}Pc(-3)]^-$ that Are Associated with the Lone Pair Orbitals of the Aza-Nitrogens and Pyrollic Nitrogens between −12 and 3 eV in the Case of ZnPc(−2)[a]

ZnPc(−2) D_{4h}	$ZnF_{48}Pc(-2)$ C_{4h}	$ZnF_{64}Pc(-2)$ C_{4h}	$(Cl^-)ZnF_{64}Pc(-2)$ C_4	$[ZnPc(-3)]^-$ C_{2v}(III)	$[ZnF_{48}Pc(-3)]^-$ C_{2v}(III)
$1b_{1g}$ −9.532	$1b_g$ −10.732	$1b_g$ −10.765	4b −8.096	$1b_1$ −6.646	$1b_1$ −8.015
$1b_{2g}$ −9.766	$2b_g$ −11.013	$2b_g$ −10.792	3b −7.983	$1a_1$ −6.767	$1a_1$ −8.177
$1e_u$ −10.013	*$1e_u$ −11.192*	*1e −11.200*	*3e −8.534*	*$2b_1$ −7.122*	*$2b_1$ −8.472*
$1e_u$ −10.018	*−11.214*	*−11.266*	*−8.603*	*$2a_1$ −7.128*	*$2a_1$ −8.486*
$1a_{1g}$ −10.817	$1a_g$ −11.985	$1a_g$ −11.984	6a −9.354	$3a_1$ −7.927	$3a_1$ −9.264

[a] The rows are ordered according to the nodal and antinodal patterns that are observed for each complex relative to the high-symmetry ZnPc(−2) parent complex. Italics are used to indicate degenerate orbitals under D_{4h} symmetry.

Table 9. Energies of the π-System MOs of ZnPc(−2), $ZnF_{48}Pc$, $[ZnPc(-3)]^-$, and $[ZnF_{48}Pc(-3)]^-$ and the Energy Difference (Δ)[a]

M_L	π MO D_{4h}	ZnPc(−2) eV	π MO C_{4h}	$ZnF_{48}Pc$ eV	Δ eV	π MO C_{2v}(III)	$[ZnPc(-3)]^-$ eV	π MO C_2	$[ZnF_{48}Pc(-3)]^-$ eV	Δ eV
8	$2a_{2u}$*	2.961	$3a_u$*	1.780	1.181	$8b_2$*	5.680	8b*	4.353	1.327
±7	$4e_g$*	2.945	$4e_g$*	1.587	1.358	$7b_2$*	5.579	7b*	4.005	1.574
		2.946		1.584	1.362	$7a_2$*	5.529	7a*	4.001	1.528
	$2b_{2u}$*	2.31	$4b_u$*	0.739	1.571	$6a_2$*	4.770	6a*	3.032	1.738
	$2b_{1u}$*	2.066	$3b_u$*	0.734	1.332	$6b_2$*	4.680	6b*	3.220	1.460
	$3e_g$*	1.677	$3e_g$*	0.029	1.648	$5b_2$*	4.147	5b*	2.372	1.783
		1.676		0.017	1.659	$5a_2$*	4.155	5a*	2.344	1.803
	$1a_{1u}$*	1.544	$2a_u$*	−0.193	1.737	$4a_2$*	3.995	4a*	2.064	1.931
	$1a_{2u}$*	0.787	$1a_u$*	−0.701	1.488	$3b_2$*	3.284	3b*	1.583	1.701
	$2e_g$*	0.736	$2e_g$*	−0.775	1.511	$4b_2$*	3.317	4b*	1.757	1.560
		0.734		−0.782	1.516	$3a_2$*	3.054	3a*	1.394	1.660
±6	$1b_{2u}$*	0.359	$2b_u$*	−1.066	1.425	$2a_2$*	2.340	2a*	0.655	1.685
	$1b_{1u}$*	0.098	$1b_u$*	−1.421	1.519	$2b_2$*	2.779	2b*	1.197	1.582
±5	$1e_g$*	−1.495	$1e_g$*	−2.824	1.329	$1b_2$*	1.434	1b*	−0.08	1.514
		−1.493		−2.829	1.336	$1a_2$*	*−2.301*	1a*	−3.899	1.598
±4	$1a_{1u}$	−5.534	$1a_u$	−6.784	1.25	$1a_2$	−3.029	1a	−4.417	1.388
	$1a_{2u}$	−8.318	$2a_u$	−9.558	1.24	$1b_2$	−5.574	1b	−6.958	1.384
	$1b_{1u}$	−8.780	$2b_u$	−10.135	1.355	$3b_2$	−6.029	3b	−7.341	1.312
	$1e_g$	−8.811	$1e_g$	−9.881	1.07	$2b_2$	−5.876	2b	−7.545	1.416
		−8.813		−9.884	1.071	$3a_2$	−6.245	3a	−7.894	1.403
	$2e_g$	−9.021	$2e_g$	−10.163	1.142	$2a_2$	−6.218	2a	−7.292	1.327
		−9.021		−10.177	1.156	$4b_2$	−6.591	4b	−7.648	1.303
	$2a_{2u}$	−9.161	$4a_u$	−10.565	1.404	$4a_2$	−6.621	4a	−8.113	1.481
	$1b_{2u}$	−9.297	$1b_u$	−9.962	0.665	$5b_2$	−6.632	5b	−7.583	0.962
	$2a_{1u}$	−9.711	$3a_u$	−10.508	0.797	$5a_2$	−7.208	5a	−8.178	0.972
±3	$3e_g$	−10.695	$3e_g$	−11.754	1.059	$6a_2$	−7.802	6a	−9.039	1.237
		−10.698		−11.761	1.063	$6b_2$	−8.076	6b	−9.257	1.181

[a] The orbitals of $ZnF_{48}Pc$ and $[ZnF_{48}Pc(-3)]^-$ are ordered in terms of the energies of the corresponding ZnPc(−2) orbital which shows the same pattern of nodes and antinodes in electron density. The orbital angular momentums associated with the orbitals located primarily on the inner cyclic polyene are shown in the left-hand column.

The $2e_g$* and $3e_g$* MOs are associated primarily with the peripheral benzene rings, while the $1a_{1u}$ orbital is associated almost exclusively with the inner perimeter, 16 atom, 18 π-electron, cyclic polyene.[11g] In the case of ZnPc(−2), there is poor orbital overlap and almost no mixing through configuration interaction (CI) with the excited state associated with the intense allowed B1 transition and the second $\pi \rightarrow \pi^*$ transition, but there is limited mixing with the $1a_{1u} \rightarrow 3e_g$* one-electron transitions which is associated primarily with the N and L bands in Gouterman's band assignment sequence, Table 1. The $1a_{1u}$ and $3e_g$* orbitals have nodes on the carbons of the inner cyclic polyene, while the $2e_g$* orbital has a set of minor nodes on the aza-nitrogens,[11g] Figure 12.

In the case of $ZnF_{64}Pc(-2)$, there is a larger predicted energy gap between the $1a_{2u}$ and the $1b_{1u}$ orbitals ($2a_u$ and $2b_u$ under C_{4h} symmetry), Table 7 and Figure 12, so the $1b_{1u} \rightarrow 1e_g$* transition which is believed to be primarily responsible for the B2 band of ZnPc(−2) is not a significant factor, Tables 1 and 5. The $1a_u \rightarrow 2e_g$* transition would be expected to have a more significant impact on the optical spectroscopy, since the electron density of the $1a_u$ significant electron density is drawn out of the inner cyclic polyene to the periphery of the π-system by the 64 fluorine atoms, Figure 15. The marked red shift and sharpening of the major bands in the B1/B2 region bands at 400 and 436 nm, compared to those of the spectrum of ZnPc(−2), are, therefore, predicted to be partially due to increased CI between the main $\Delta M_L = \pm 1$ allowed B1 excited state and the lower energy second $\pi \rightarrow \pi^*$ ($1a_{1u} \rightarrow 2e_g$*) excited state. It should be noted, however, that the INDO/s calculation actually predicts enhanced CI between $2a_u \rightarrow 1e$* and $1a_u \rightarrow 3e_g$* rather than between $2a_u \rightarrow 1e_g$* and $1a_u \rightarrow 2e_g$* in the case of $ZnF_{64}Pc(-2)$.

The presence of Cl^- as an axial ligand is probably a major factor in the marked red shift of the major bands within the B1/B2 region bands relative to that typically observed for MPc(−2). It has been observed previously that the presence of CN^- as an axial ligand results in a marked splitting of the B1 and B2 bands.[11a,f,g,17b,d] The major nodal positions of the $1a_{2u}$ orbital of MPc(−2) are located on the aza-nitrogens and pyrollic nitrogens which are coordinated to the central metal ion.[11g] In contrast, those of the $1a_{1u}$ orbital are located on the eight carbon atoms of the inner cyclic polyene. The presence of a Cl^- axial

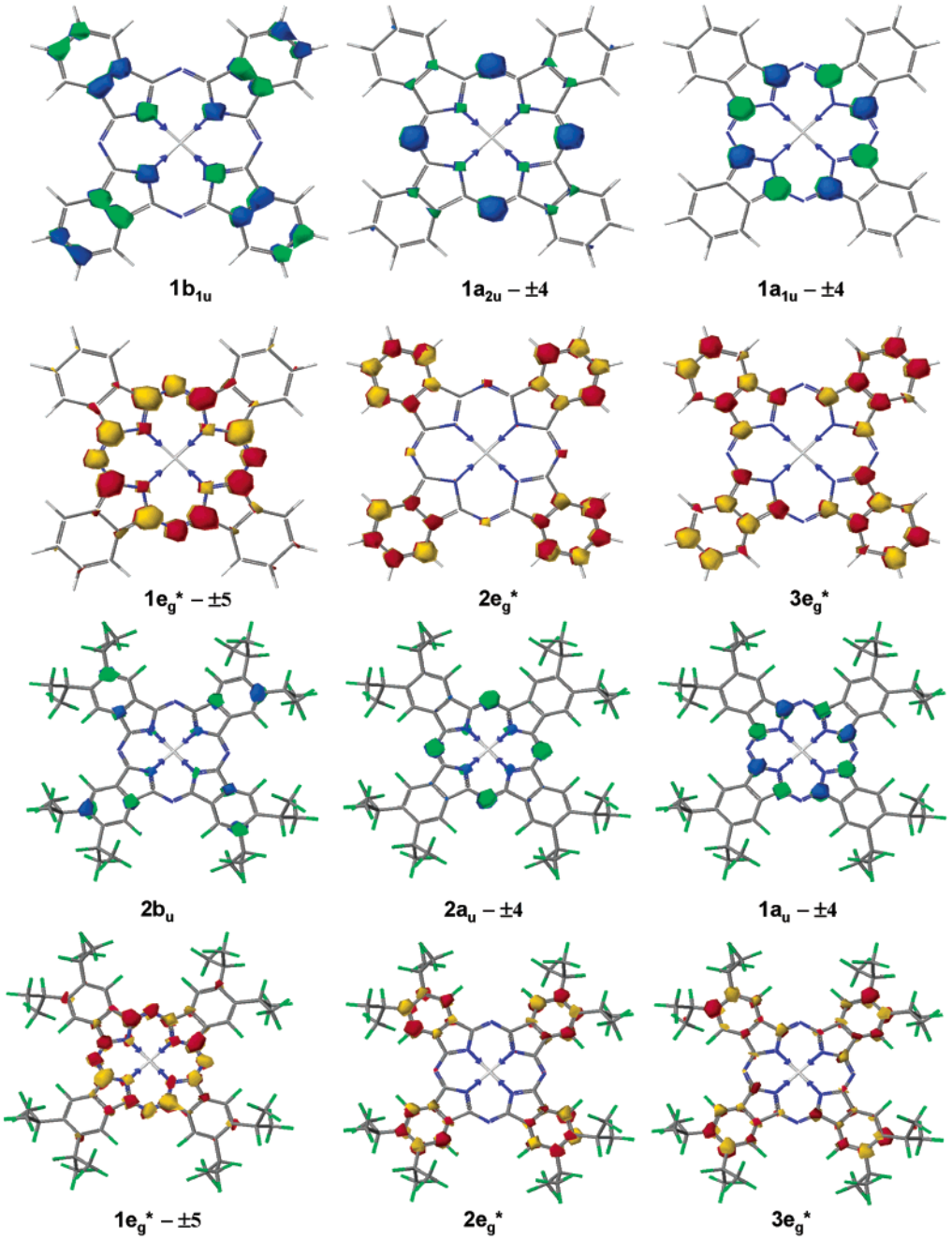

Figure 12. Electron density contour maps of the three highest HOMOs and three lowest LUMOs arranged in ascending energy for the frontier π-system molecular orbitals of the D_{4h} symmetry ZnPc(−2) (top two rows) and C_{4h} symmetry $ZnF_{64}Pc(-2)$ (bottom two rows) that are associated with the major $\pi \rightarrow \pi^*$ transitions in the UV−visible region, Tables 1, 5, and 7. The images were generated by the CAChe Tabulator program on a molecular outline at the 0.05 energy au level of the isosurface value of the electrostatic potential. The green and blue shading of the HOMOs and the red and yellow shading of the LUMOs represent the two phases visible from one face of the ring. The peripheral fluorines are colored green.

ligand would therefore be expected to have a much greater influence on the energy of the B1 transition than on the Q transition, since the pyrollic nitrogens are coordinated with the central metal ion. In the case of $(Cl^-)ZnF_{64}Pc(-2)$, the B1 band is predicted to red shift significantly, Table 6. The predicted reduction in CI between the B1 excited state and the higher energy excited states in the UV region would also account for the marked sharpening of the major bands observed at 400 and 436 nm.

Optical Spectra of $[ZnF_{64}Pc(-3)]^-$. The lack of temperature dependence observed in the MCD spectrum of $[ZnPc(-3)]^-$ [11c,30] and $[ZnF_{64}Pc(-3)]^-$, Figure 12, is unambiguous evidence that the MCD spectrum is completely dominated by B terms (rather than the temperature dependent C terms). Band deconvolution carried out on both the absorption and MCD spectral data, Figures 17 and 18, requires a large number of individual bands. Like the fits required for the $[ZnPc(-3)]^-$ reported previously,[11c] only MCD B terms were used, and in every case, removal of one of the bands resulted in significantly reduced fitting quality. In the fitting carried out here, the band parameters are used in both the absorption and MCD spectral data.

A ^2E ground state would have been anticipated under the C_4 symmetry observed in the case of $(Cl^-)ZnPc(-2)$, Table 6, so

(30) Mack, J.; Kirkby, S.; Ough, E. A.; Stillman, M. J. *Inorg. Chem.* **1992**, *31*, 1717.

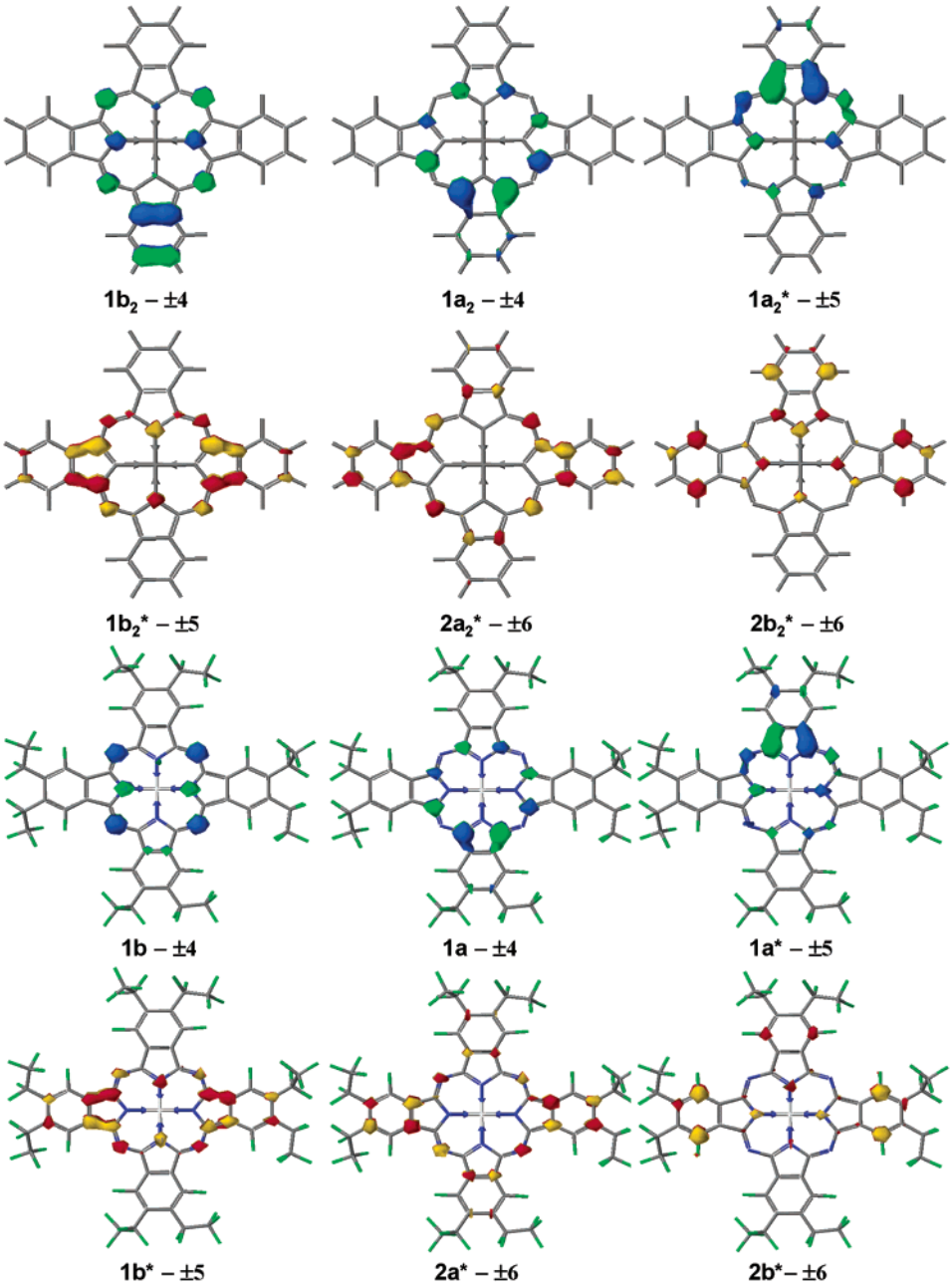

Figure 13. Electron density contour maps of the three highest HOMOs and three lowest LUMOs arranged in ascending energy for the frontier π-system molecular orbitals of C_{2v}(III) symmetry $[ZnPc(-3)]^-$ (top two rows) and $[ZnF_{48}Pc(-3)]^-$ species (bottom two rows) that are associated with the major $\pi \rightarrow \pi^*$ and $\pi^* \rightarrow \pi^*$ transitions in the UV−visible region, Tables 3, 4, and 7. The images were generated by the CAChe Tabulator program on a molecular outline at the 0.05 energy au level of the isosurface value of the electrostatic potential. The green and blue shading of the HOMOs and the red and yellow shading of the LUMOs represent the two phases visible from one face of the ring. The peripheral fluorines are colored green.

there must be a substantial static Jahn−Teller splitting of the ground state. In the absence of X-ray crystallographic data, $[ZnPc(-3)]^-$ was assumed to have C_{2v}(III) symmetry, since the MOs obtained from the ZINDO calculations would have C_{2v}(III) properties[31] if ring saddling occurs due to the loss of aromaticity,[11c] Figure 16. Axial ligation is not expected to induce significant ring distortions, thus leaving the electron addition as the only reason that can account for this ring saddling. Under C_{2v}(III) symmetry, the C_2 axis of MPc(−2) lies in the plane of the ring and thus does not correspond to the C_4 symmetry axis of MPc(−2). Michl[32] has demonstrated that when the symmetry of cyclic polyene complexes is reduced below D_{4h}, the derivative-shaped, *x*/*y*-polarized A terms are replaced by intense, coupled pairs of *x*- and *y*-polarized, Gaussian-shaped B terms of opposite sign. The polarization of the coupled bands are *x* and *z* in the case of the C_2 and C_{2v}(III) symmetry of $[ZnF_{48}Pc(-3)]^-$ and $[ZnPc(-3)]^-$ where the major symmetry axis does not match that of D_{4h}, Figure 16. The band polarizations do not determine the sign of the B terms; rather, the sign is due to the relative orbital angular momenta of the ground and excited states in the absence of the perturbation to the molecular symmetry. When there is a static Jahn−Teller distortion of the partially

(31) Donini, J. C.; Hollebone, B. R.; Lever, A. B. P. *Prog. Inorg. Chem.* **1977**, *22*, 225.

(32) (a) Michl, J. *J. Am. Chem. Soc.* **1978**, *100*, 6801. (b) Michl, J. *Pure Appl. Chem.* **1980**, *52*, 1549.

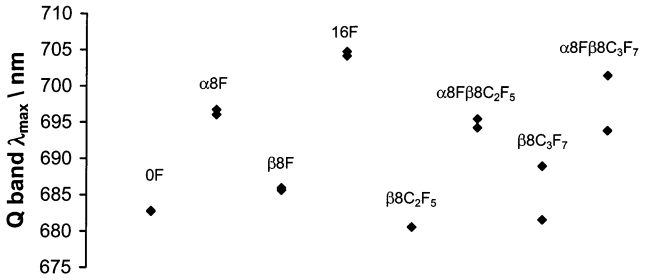

Figure 14. Effect on the λ_{max} of the Q-band of ZnR′8R″8Pc(−2) of subsitution with R′ = H and F and R″ = H, F, $-C_2F_5$, and *i*-C_3F_7 at the α- and *β*-positions, respectively. The geometries for α8F, *β*8F, 16F(α8F*β*8F), *β*8C_2F_5, α8F*β*8C_2F_5, *β*8*i*-C_3F_7, and α8F*β*8*i*-C_3F_7 complexes were optimized using the MOPAC software package within the CAChe Workspace, and the UV−visible spectra were calculated using the INDO/s Hamiltonian.

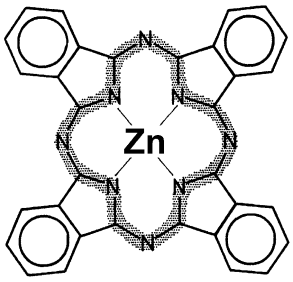

Figure 15. Diagram showing the 16-atom, 18-*π*-electron polyene system of ZnPc complexes that is the basis for the four-orbital model of Gouterman.

filled $1e_g$* LUMO in an $[MPc(-3)]^-$ species, generated by the addition of an electron to the two orbitals of the Jahn−Teller split LUMO of MPc(−2), there are three possible spin-allowed electronic configurations that explain the Q, B1, and B2 $\pi \rightarrow \pi^*$ transitions of the MPc(−2) species, Tables 3 and 4 and Figure 9. Only two spin-allowed electronic transitions are possible for the main $\Delta M_L = \pm 1$ allowed $\pi^* \rightarrow \pi^*$ transition out of the Jahn−Teller split $1e_g$* LUMO of the inner cyclic polyene to the set of symmetry split orbitals that would be a $1e_u$* orbital if only the inner cyclic polyene were considered. The coupled negative and positive B terms arising from these $\pi^* \rightarrow \pi^*$ bands are expected to have similar intensities, since the B terms that arise from field-induced mixing of close-lying states should sum to zero. This equivalence in intensity is not anticipated between the three coupled negative and positive B terms arising from the major $\pi \rightarrow \pi^*$ transitions. An intense B term is expected to be followed at higher energy by two weaker B terms of the opposite sign. The bands at 958/925/880 and 635/569 nm in the $[ZnPc(-3)]^-$ spectrum were assigned to the Q and $\pi^* \rightarrow \pi^*$ transitions on this basis, since they matched the B term intensity patterns anticipated to arise from the lowest energy $\pi^* \rightarrow \pi^*$ and $\pi^* \rightarrow \pi^*$ transitions.

In the case of $[ZnF_{48}Pc(-3)]^-$, the ZINDO calculation predicts an increased separation between the LUMO+1 and LUMO+2 orbitals that are involved in the $\pi^* \rightarrow \pi^*$ transition, Tables 3 and 4. Consequently, a larger energy gap would be

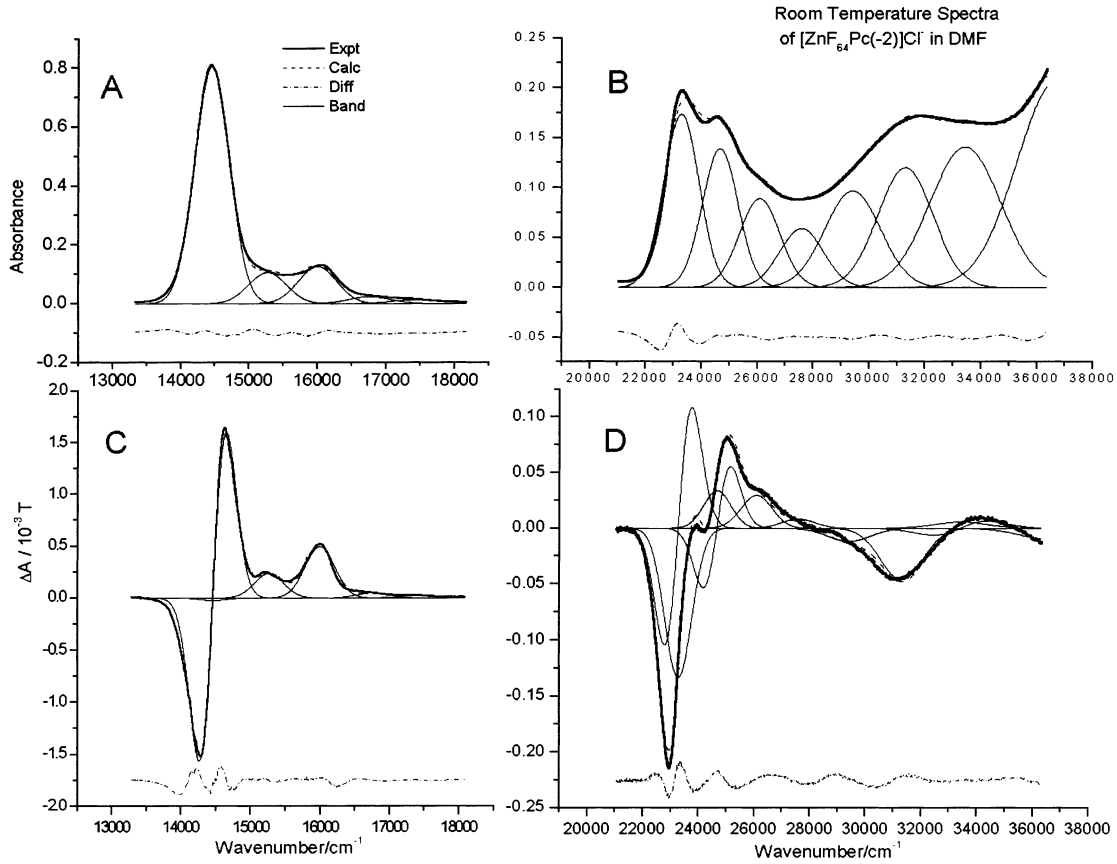

Figure 16. Band deconvolution analysis of the absorption and MCD spectra of $ZnF_{64}Pc(-2)$ in the Q (A and C) and B1/B2 (B and D) regions. The residuals between the fitted and experimental lines are shown under the spectral data. The fitting was carried out by connecting the band parameters in both absorption and MCD spectra, both A terms and B terms were used. A coupled B term was always added when A terms were included in the fit. The number of bands used in the Q-band vibrational region between 15 000 and 17 000 cm^{-1} does not reflect the actual number of individual bands present. In all other regions, the number of bands used is the minimum necessary to reduce the residuals in both absorption and MCD data. The energies of the positive A terms used in this fit are shown in Figure 18.

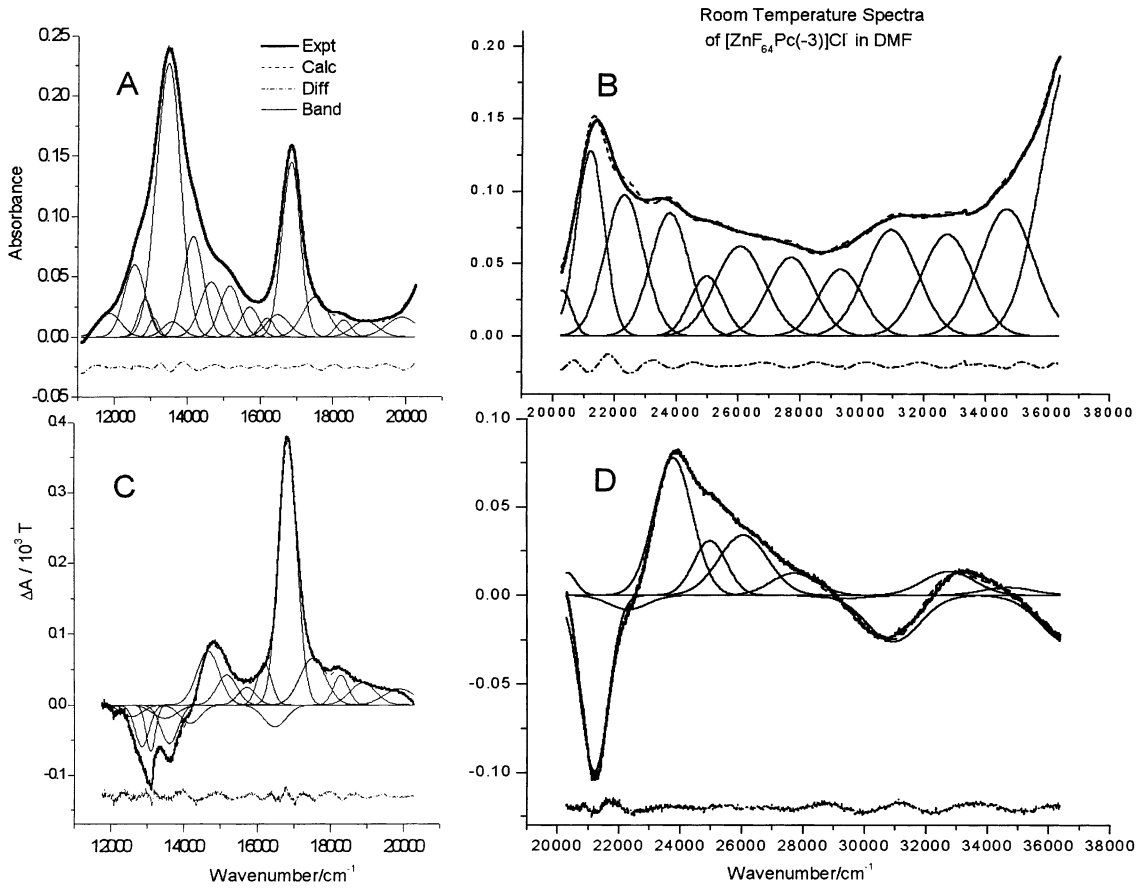

Figure 17. Spectral band deconvolution analysis of the absorption and MCD spectra of $[ZnF_{64}Pc(-3)]^-$. The residuals between the fitted and experimental lines are shown under the spectral data. The fitting was carried out by connecting the band parameters in both absorption and MCD spectra; only B terms were used. The number of bands used in the region between 11 000 and 20 000 cm^{-1} is the minimum necessary to reduce the residuals in both absorption and MCD data. The energies of all the B terms used in this fit are shown in Figure 18.

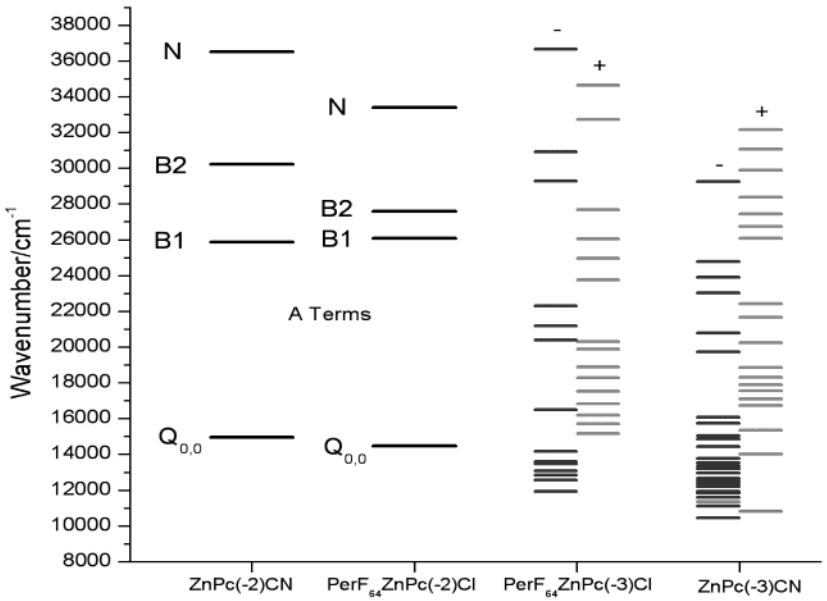

Figure 18. A stacked plot showing the energies of the A terms used in the fits of the absorption and MCD spectral data for $(CN^-)ZnPc(-2)$[16a,b] and $(Cl^-)ZnF_{64}Pc(-2)$ and the B terms used in the fits of the data for the ring-reduced $[(Cl^-)ZnF_{64}Pc(-3)]^-$ and $[ZnF_{64}Pc(-3)]^-$. The signs of the B terms are indicated by the position of the energy bar; left represents negative B terms, and right represents positive B terms.

anticipated in the two B terms. A large splitting in the $\pi^* \rightarrow \pi^*$ B terms has previously been observed in the spectrum of $[ZnTPP(-3)]^-$.[33] The sequence of two negative and three positive B terms, identified between 550 and 800 nm, Figure 17, can therefore be assigned to overlapping bands arising from the Q and $\pi^* \rightarrow \pi^*$ bands. This overlap occurs because of the blue and red shifts of the Q and $\pi^* \rightarrow \pi^*$ bands, respectively. The bands at 429 and 475 nm can be assigned primarily to the

B1 transition. The red shift and band sharpening relative to $[ZnPc(-3)]^-$, which are similar to those observed in the case of $ZnF_{64}Pc(-2)$, are again probably due to increased configuration interaction with the second $\pi \rightarrow \pi^*$ ($1a_{1u} \rightarrow 2e_g^*$ in the case of $MPc(-2)$) transition rather than with higher energy excited states. This interaction would also account for the drop in intensity observed in the 300−400 nm region.

The failure to photooxidize $(Cl^-)ZnF_{64}Pc(-2)$ is in stark contrast with (i) the behavior of nonfluorinated $ZnPc(-2)$, for which the photooxidation reaction results in the formation of a $[ZnPc(-1)]^+$ species and (ii) the notion that up to four additional electrons can be reversibly added or two reversibly removed from the phthalocyanine π-system.[11b] ZINDO calculations (Table 7), however, support our observations by predicting a relative stabilization of the molecular orbitals of the π-system of $ZnF_{64}Pc(-2)$ of over 1 eV.

Conclusions

The introduction of eight bulky, *i*-C_3F_7 groups at the periphery of the Pc ring facilitates the study in solution by enhancing solubility. The electron withdrawing properties of the substituents has a substantial impact on the π-system of the ligand, which is strongly reflected in changes in the redox properties of $ZnF_{64}Pc(-2)$. Ring oxidation is not possible using the conventional chemical, photochemical, and electrochemical approaches developed for $ZnPc(-2)$. Importantly, the $[ZnF_{64}Pc(-3)]^-$ anion radical can be easily produced and is usually present in equilibrium with the neutral complex and exhibits a remarkable stability for an oxygen-sensitive paramagnetic species. The optical spectra of both $ZnF_{64}Pc(-2)$ and $[ZnF_{64}Pc(-3)]^-$ are also markedly different from those of the unsubstituted $ZnPc(-2)$ and $[ZnPc(-3)]^-$ species, consistent with the notion that the electron withdrawing influence of the peripheral substituents effects the π MO to differing extents. The B1 and Q-bands are red shifted; the location of the latter in the red region of the visible spectrum, combined with the chemical resistance imparted by the perfluoroalkyl substituents, suggests possible future applications in photobiology, such as photodynamic therapy.[10] The chemical stability of both the neutral and anion radical species could also be exploited for catalytic purposes.[9,19] Other peripheral R_F substituents are likely to have a major impact on the electronic structure of the Pc π-system and thus could be used to design new complexes with a specific set of properties suited to new applications.

Acknowledgment. We thank NSERC of Canada for operating and equipment funds (to M.J.S.), Wen Jun Han for help with the electrochemistry, the Society of Porphyrins and Phthalocyanines for travel funds (to S.K.) to the ICPP-2 conference in Kyoto to present preliminary results of this work, CAChe Fujitsu America for use of the latest software packages, Prof. Lars Konermann at U. W. O. for use of the mass spectrometer, and the Canadian Foundation for Innovation for funding (to L.K.). We also thank the Solomon Foundation and Air Products and Chemicals for financial support (to S.M.G.).

JA0299710

(33) Mack, J.; Stillman, M. J. *J. Porphyrins Phthalocyanines* **2001**, *5*, 67.